Naval Research Laboratory
Washington, DC 20375-5320

Computational Study of Shock-Associated Noise Characteristics Using LES

JUNHUI LIU
ANDREW CORRIGAN
K. KAILASANATH

Laboratory for Propulsion, Energetic, and Dynamic Systems
Laboratories for Computational Physics and Fluid Dynamics

PABLO MORA
NICHOLAS HEEB
EPHRAIM GUTMARK

University of Cincinnati
Cincinnati, Ohio

October 3, 2014

REPORT DOCUMENTATION PAGE

1. REPORT DATE (DD-MM-YYYY) 03-10-2014	2. REPORT TYPE Memorandum Report	3. DATES COVERED (From - To) April 2013 – March 2014

4. TITLE AND SUBTITLE

Computational Study of Shock-Associated Noise Characteristics Using LES

5a. CONTRACT NUMBER

5b. GRANT NUMBER

5c. PROGRAM ELEMENT NUMBER

6. AUTHOR(S)

Junhui Liu, Andrew Corrigan, K. Kailasanath, Pablo Mora,[1] Nicholas Heeb,[1] and Ephraim Gutmark[1]

5d. PROJECT NUMBER

5e. TASK NUMBER

5f. WORK UNIT NUMBER
64-9290-C-4

7. PERFORMING ORGANIZATION NAME(S) AND ADDRESS(ES)

Naval Research Laboratory
4555 Overlook Avenue, SW
Washington, DC 20375-5344

8. PERFORMING ORGANIZATION REPORT NUMBER

NRL/MR/6040--14-9560

9. SPONSORING / MONITORING AGENCY NAME(S) AND ADDRESS(ES)

Office of Naval Research
One Liberty Center
875 North Randolph Street, Suite 1425
Arlington, VA 22203-1995

10. SPONSOR / MONITOR'S ACRONYM(S)

ONR

11. SPONSOR / MONITOR'S REPORT NUMBER(S)

12. DISTRIBUTION / AVAILABILITY STATEMENT

Approved for public release; distribution is unlimited.

13. SUPPLEMENTARY NOTES

[1]University of Cincinnati, 2600 Clifton Avenue, Cincinnati, Ohio 45221-0070

14. ABSTRACT

The shock-associated noise characteristics of an underexpanded jet at three jet temperatures were investigated using large-eddy simulations (LES). The impact of shock cells on the flow field and near- and far-field noise characteristics were examined. The impact of shock-associated noise is confined to one and a half jet core length in the near field. The near-field shift of the shock-associated peak frequency matches well with the inverse of the shock-cell size, indicating that the variation of the shock-cell size is largely responsible for this shift. In the far field, the variation of the shock-associated peak frequency agrees well with the available empirical model over a large range of the radiation angle, but the model under-predicts the fast increase near the end of the shock-associated noise region. In addition, the distributed nature of the shock-associated noise source impacts the far-field noise characteristic if the distance is not sufficiently large. Heating decreases the shock-cell impact on the total noise, but the heating impact on the shock-associated noise level in the upstream direction is opposite to that in the downstream direction. On the other hand, heating greatly increases the mixing noise, reducing the difference between the shock-containing jets and the shock-free jets.

15. SUBJECT TERMS

CFD	Shock-associated broadband noise	Military flight noise
Large-eddy simulations	Screech tone	Supersonic jet flows
Jet noise	Mixing noise	Nozzle flows

16. SECURITY CLASSIFICATION OF:			17. LIMITATION OF ABSTRACT	18. NUMBER OF PAGES	19a. NAME OF RESPONSIBLE PERSON Junhui Liu
a. REPORT Unclassified Unlimited	b. ABSTRACT Unclassified Unlimited	c. THIS PAGE Unclassified Unlimited	Unclassified Unlimited	33	19b. TELEPHONE NUMBER (include area code) (202) 767-6590

CONTENTS

COMPUTATIONAL STUDY OF SHOCK-ASSOCIATED NOISE CHARACTERISTICS USING LES

I. INTRODUCTION

The noise generated by high performance, supersonic military aircraft during takeoff or landing is dominated by jet noise, which includes both mixing and shock-associated noise components. Since the engine exhaust of military aircraft is inevitably hot and the shock-associated noise can have a substantial contribution to the overall noise level, understanding the characteristics of the shock-associated noise and its contribution to the overall sound pressure level at both cold and heated jet conditions is important to the development and optimization of effective noise reduction techniques. The characteristics of shock-associated noise have been experimentally and theoretically investigated over several decades. The early investigations, for example Refs [1]-[11], have laid a solid foundation for improving the understanding of shock-associated noise characteristics. It is established that shock-associated noise, which includes both discrete tones (screech) and broadband noise components, is generated by the weak but coherent interaction between downstream propagating turbulence in the shear layer and shock cells in the jet plume [2]. The peak frequency of the broadband shock-associated noise component is a function of the shock-cell spacing, the convection velocity of the shear-layer turbulence and the observation angles [1][2]. The intensity of the broadband shock-associated noise is a strong function associated with the degree of the off-design condition, $\sqrt{\left|M_j^2 - M_D^2\right|}$, where M_D is the nozzle exit Mach number and M_j the fully expanded Mach number. In addition, shock-associated noise radiation is understood as omnidirectional [3], whereas the mixing noise is radiated principally in the downstream direction. Thus, the importance of the shock-associated noise is more prominent in the upstream direction of the nozzle, but less in the downstream direction. Furthermore, the shock-associated noise has a much weaker dependence on the jet temperature than the mixing components [2][3]. This means that the shock-associated noise may dominate the total noise at the cold jet condition, but its importance could be smaller under highly heated jet conditions [3].

Theoretical models have been developed to calibrate broadband shock-associated noise. The sources are modeled as phased array monopoles located at the tips of the shock cells by Harper-Bourne and Fisher [1] and as pressure waveguides that interact with downstream propagating instability waves by Tam and Tanna [2] and Tam [4]. In addition, a noise model using an acoustic analogy based on the linearized Euler equations has been developed by Morris and Miller [12] and the equivalent source terms depend on the averaged properties of turbulence and shock cells, which are computed from Reynolds-averaged Navier–Stokes solutions to overcome the limitations and empiricism present in previous broadband shock-associated noise models. Furthermore, Viswanathan, Alkislar and Czech [13] have applied scaling laws to examine the characteristics of the broadband shock-associated noise. The shock-associated noise contribution was separated from the mixing noise contribution by using a scaling methodology developed for mixing noise. This methodology is based on the observation that the turbulent mixing noise is unaffected by the presence of shocks in the jet plume as long as there are no strong screech tones [14]. They found that the shock-associated noise intensity is first increased as the jet temperature increases, but it saturates with further jet temperature increase. They also found that shock noise intensity does not scale exactly as the fourth power of $\sqrt{\left|M_j^2 - M_D^2\right|}$ in the forward quadrant as assumed in the past [3], but the power spans a range from 2.9 to 6.17, depending on the radiation angle and the jet temperature ratio. The heating effect on the broadband shock-associated noise has been recently investigated by Kuo, McLaughlin and Morris [15]. In this study, helium-air mixtures were used to simulate the jet-heating effect. Although the shock noise intensity only weakly depends on the jet temperature, they found that the simulated heating impact on underexpanded and overexpanded jet conditions shows an opposite trend; the peak broadband shock-associated noise level in underexpanded jets decreases with decreasing jet density,

but the reverse is true for over-expanded jet conditions. In addition, the peak frequency of underexpanded conditions increases with the simulated jet temperature, but the overexpanded jet conditions show a decreased peak frequency.

The investigation of shock-associated noise has been carried out mostly by far field measurements. Some near-field measurements have also been made, but most measurements were at cold jet conditions. An early example is the work of Seiner and Yu [10], and more recent examples can be found in Refs [16]-[20]. Seiner and Yu provided evidence for the existence of some large-scale flow structures that collectively interact and phase the motion of the downstream shocks. It was found that the broadband peak of the near-field pressure spectra shifts to higher frequency in the downstream direction and the downstream shock cells dominate shock noise production. This peak frequency shift has also been observed recently, for example, by Andre et al. [16] and Savarese et al. [17]. Seiner and Yu identified the Doppler effect as the cause of this peak frequency shift in the near field. Furthermore, Bridges and Wernet [18] have studied turbulence statistics associated with broadband shock-associated noise using time-resolved particle image velocimetry to a series of jet flows, including three Mach numbers and different total temperatures. They found that the mean and turbulence quantities of fully expanded heated jets collapse well when the coordinates are normalized with the jet potential core length, and the heating effect has a negligible effect on the shock structure, but it shortens the potential core and causes the half-velocity point to move inward. The strong screech tones observed in their measurement have a large influence on the mean and turbulence development, but if the screech tones are suppressed, the shock cells have little impact on the jet core length and turbulence level, and the low-frequency mixing noise is not affected by the presence of shock cells.

Although significant progress has been made in the investigation of the characteristics of shock-associated noise by using experimental approach and theoretical modeling, few studies have been made using large-eddy simulations (LES). One such effort was made by Bodony, Ryu and Lele [21], who investigated the shock-associated noise characteristics by comparing jet flows of an underexpanded jet and a perfectly matched jet. An actual nozzle geometry was not used in the simulations. Instead, an inflow boundary with a hyperbolic tangent velocity profile and the first three modes of the multiple scales solution were used for the underexpanded jet. They found that the off-design jet had a longer potential core length with reduced levels of axial velocity fluctuations. They also observed that the near-field pressure of the off-design jet was dominated by Mach wave radiation in the upstream portions of the flow field but eventually relaxed to a state more similar to the on-design jet.

In this work, we use an unsteady compressible flow solver provided by the Jet Engine Noise Reduction (JENRE) code, which has been developed for the simulation of supersonic jet flow and its acoustic properties, based on the MILES (Monotonically Integrated Large-Eddy Simulation) [22] approach. In addition, the far-field noise levels are predicted by using the Ffowcs Williams & Hawkings (FW-H) method [23]. In this paper, jet flows at an underexpanded jet condition with three jet total temperature are considered. It is ideal to construct both shock-containing and shock-free jets to investigate the shock-associated noise, so shock-free jet flows with the same fully expanded jet conditions are also simulated.

II. METHODOLOGY IN JENRE

JENRE is built on a general framework that includes support for different types of numerics, including both cell-centered finite volume and nodal finite element methods. Since a Taylor-Galerkin finite element method maintains second order spatial accuracy even on tetrahedral grids, we employ the Finite Element Flux Corrected Transport (FEM-FCT) method ([24]-[27]) in this paper. To improve efficiency, an edge-based formulation is used for all flux integration and limiting calculations [28]. In addition, the Zalesak multi-dimensional flux limiter [29] is used and the flux limiter that synchronizes the minimum of the limiter obtained for the density is employed. The multi-dimensional FCT flux limiter

provides an implicit subgrid stress model, which ensures monotonicity at shocks and sharp features with minimal artificial dissipation. In addition, JENRE supports hybrid grids consisting of both unstructured with arbitrary cell types, and structured hexahedral blocks. In this paper, however, only tetrahedral grids are used for its simplicity and the accurate representation of complex geometries.

Since realistic supersonic jet noise simulations require highly detailed physics, complex geometry, large grid sizes, and fast turn-around times, JENRE has been developed with an emphasis on high computational performance and the ability to exploit emerging massively parallel, high-performance computing (HPC) architectures. In addition to improving raw performance, JENRE implements multiple levels of parallelism. The first level is fine-grained, shared-memory parallelism using multi-core CPUs or many-core GPUs (Graphics Processing Units). The second level is coarse-grained, distributed-memory parallelism, domain decomposition with inter-processor communication being handled using MPI (Message Passing Interface). Since these two forms of parallelism are complementary, JENRE can be compiled and run on either a cluster of multi-core CPUs or multi-core GPUs. In this paper, the MPI version of the CPU code is used.

III.   NOZZLE GEOMETRY AND COMPUTATIONAL DOMAIN

The nozzle geometry for the shock-containing jet flows is shown in Figure 1. It is the same converging-diverging (C-D) nozzle as reported in Refs. ([20], [30]), They are representative of practical military engine nozzles, which do not have smoothly varying contours designed by the method of characteristics to produce shock-free jet flows at the design condition. Instead, they typically have a conical converging section, a sharp throat and a conical diverging section, which allows the area ratio to be changed in flight to adapt to local conditions and thrust requirements. The design Mach number of this C-D nozzle is 1.5, and the fully expanded pressure ratio is 3.7. In this paper an underexpanded jet with the nozzle pressure ratio of 4.0 is used. Three total jet temperatures T_o/T_{amb} = 1.0, 2.0, and 3.0 are studied, where T_o is the total temperature inside the nozzle and T_{amb} is the ambient temperature. Since the jet flows from this type of C-D nozzle are not shock free even at the perfectly matched jet condition ([20], [30]), the shock-free jet flows are made by specifying Dirichlet boundary conditions at the nozzle exit plane, where the fully expanded jet conditions of the shock-containing jet flows are used.

Figure 2(a) shows the computational domain, where the useful near-field region is enclosed by the nozzle surfaces and a funnel-shaped surface. This funnel-shaped surface is also used as the FW-H integral surface for the far-field noise prediction. The mesh beyond the useful near-field region increases quickly, so only the data in the useful region will be used in the analysis. The axial range of the funnel-shaped surface extends from 2D (D is the nozzle exit diameter) upstream of the nozzle exit to 27D downstream. The upstream portion has a radius of 1.5D, but the downstream portion is at 9.5° to the axial axis. Since the shear layer is thin, very fine cell sizes are needed to resolve the shear layer. Hence two grid resolutions with cell sizes of D/286 and D/143 are tested in the shear layer region. Because the turbulence structures grow in size as they propagate downstream, the cell size gradually increases in the axial direction to a size around D/30. The cell size distributions along the lip line are shown in Figure 2(b), where both meshes are presented. In these two meshes, the cell size of D/30 extends to the region enclosed by the black lines shown in Figure 2(a). The radius of this region is 1.1D above the nozzle exit and 1.8D from x = 10D to 25D. Furthermore, the cell size gradually increases to a size around D/20 in the region near the funnel-shaped surface, beyond which the cell size increases quickly to a very large size in the far field. Overall the simulation domain extends to 30D in the radial direction, 17D upstream of the nozzle exit and 70D downstream in the axial direction. A buffer zone is implemented near the far-field boundaries to remove the wave reflection, and the number of grid points is 51 million for the coarser mesh and 59 million for the fine mesh. Since the current Reynolds number exceeds 10^6, the impact of the nozzle boundary layer is expected to be small [11], and thus, it is not computed and free-slip boundary conditions are used on the nozzle surface.

IV. IMPACT OF SHOCK CELLS AND HEATING ON THE FLOW FIELD

Figure 3 shows the comparison of the shock-cell structure and shock-cell location near the nozzle exit between LES predictions and the experimental PIV measurement [20]. It can be seen that the shock-cell structures and shock-cell locations predicted by both the fine and coarser meshes agree very well with the measurement data. However, the coarser mesh predicts a slower initial growth rate of the shear layer, indicating the transition from the laminar to the turbulent shear layer is slower than that shown in the measurements. On the other hand, the fine mesh predicts a transition similar to that observed in the PIV measurement, and thus the fine mesh is used for all the simulations discussed in this paper.

The total pressure and total temperature distributions along both the centerline and an axial line near the jet axis are shown in Figure 4. There is a Mach disk impacted region near the jet axis with a small radius, as shown in Figure 3, and the radial variation is very large across the jet center. To avoid impact of the Mach disk, data along an axial line with a small deviation, 0.1D, from the jet axis is also used, such as that shown in Fig. 4(a), where the experimental data is measured by using a Pitot probe. Since a normal shock wave is present in front of the probe when the local flow is supersonic, the Rayleigh Pitot probe formula [31] was applied to the simulation results to account for the normal shock wave correction. The agreement of the shock-cell structure and location with the experimental data is very good up to the fifth cell for both meshes, after which shock cells begin to decay quickly. LES predictions agree with each other very well, but they show a slower decay than the measurement and a slightly longer core by roughly 0.8 D. Figure 4(b) and (c) show the comparison between simulation results and the measurement data at a heated jet condition of T_o/T_{amb} = 2.0. The nozzle diameter in measurements is 0.813", smaller than that used in simulations. Numerical results of the total pressure predicted along both the centerline and the axial line with 0.1D off the jet axis are presented, whereas the measurement data only have the centerline results. It can be seen that the Mach disk causes a large radial variation on the total pressure near the jet axis, and a very small distance from the jet axis introduces a significant difference to the magnitude. This sensitivity makes the measurement very difficult, because it needs much care to align the probe exactly on the jet axis. It appears that the measurement data are closer to the data along the axial line with r = 0.1D, indicating that probes may have not been exactly positioned on the jet axis. On the other hand, the total temperature is less sensitive to the Mach disk impact and both predictions agree with each other very well.

Figure 5 shows the time-averaged streamwise velocity distributions for both shock-containing and shock-free jets at three total jet temperatures, and Figure 6 shows the axial velocity and total temperature centerline distributions. The shock-containing and shock-free jets show similar jet core lengths at these three jet temperatures. This shows that shock cells have little impact on the jet core length, which is consistent with the observation in Ref. [18]. On the other hand, the heating effect shows a much larger impact. Increasing the jet temperature increases the initial shear layer growth rate, and reduces the jet core length. The heating effect, however, does not affect the shock cells upstream of the jet decay region. These trends agree with well-established observations, for example, as reported in Ref. [18] and [32].

Figure 7 shows power spectral density (PSD) distributions of the axial velocity along the lip line of the cold shock-containing jet. It can be seen that the energetic frequencies decrease in the axial direction, indicating that length scales increase in the downstream direction. There is a small region around x = 1D that has substantial energy in the high-frequency range. This region is followed by a quick decrease of the energetic frequencies and then an almost logarithmic decrease downstream of x = 3D. In addition, the axial profiles present an inertial range with the slope of -5/3, and the inertial range shifts to lower frequency in the downstream direction, because turbulence scales increase in size downstream. Figure 8 shows the time-averaged turbulence kinetic energy distributions along both the centerline and the lip line in both shock-containing and shock-free jet flows at three jet temperatures. It can be seen that shock cells increases the turbulence kinetic energy along the centerline in the region where shock cells are present. It appears that the shock cells almost superimpose their contribution on the shock-free distribution. The impact on the lip line, however, is small except the region upstream of 4D, possibly because shock cells

become smaller downstream and move away from the lip line. There is a large peak near the nozzle exit at roughly x = 1D, which may be generated by the transition from laminar to turbulence near the nozzle exit. This large peak is dominated by high-frequency components as shown in Figure 7. In addition, since the heating effect impacts both the jet core length and the initial shear-layer growth as shown in Figure 5 and 6, it is expected that the heating effect would impact the distribution of the turbulence kinetic energy accordingly. Figure 9 shows the heating impact on the turbulence kinetic energy distributions, where the axial location is normalized by the nozzle exit diameter D and the potential jet core length. The potential jet core length (Lc) of the shock-free jets are 10.1D, 8.5D, and 8.33D, respectively, at T_o/T_{amb} = 1.0, 2.0 and 3.0 based on the location of $0.95U_j$ in each case. Since the overall trend of shock-containing and shock-free distributions is very similar, only shock-free results are shown in Figure 9. It can be seen that the turbulence kinetic energy distributions collapse well when the x coordinate is normalized with the jet potential core length. The peak of the centerline distribution is roughly located at 1.5Lc, and the heating effect slightly increases peak levels of both the lip line and centerline. Near the nozzle exit the two heated cases show a faster initial increase, which is consistent with the faster initial shear-layer spreading shown in Figure 5 near the nozzle exit.

V.   IMPACT OF SHOCK-CELLS AND HEATING EFFECT ON NEAR-FIELD ACOUSTIC CHARACTERISTICS

Figure 10 shows the comparison of the near-field overall sound pressure level (OASPL) along the FW-H integral surface using both the coarser and finer meshes and also the data from measurements in Ref. [20]. The coarser mesh prediction is similar to that of the fine mesh. The difference is within 1.5dB upstream of x = 5D, and very small further downstream. Both predictions and the measurement data show a small peak located around x = 4D, where the fine mesh predicts a lower level than the coarser mesh, but the measurement data is between these two. In addition, the magnitude and the overall trend predicted by both meshes agree well with the measurement data. The largest difference between the fine mesh prediction and the measurement data is around 2dB. The overall peak location in LES predictions is near the end of the potential core (x = 10D), but the measurement shows a peak location 1D further downstream at x = 11D. The total time lengths of LES data used for the spectral analysis are around 900 D/U$_j$, which are divided into six windows and 50% overlap is used between each window. This results in 11 windows and each window has 4096 points. The frequency resolution is scaled up to 50Hz, which is the resolution used in the experimental measurements. Figure 11 shows the comparison of sound pressure levels (SPL) at four near-field locations on the FW-H surface. The first location is above the nozzle exit, and the second and the third locations shown in Figure 11(b) and (c) are in the region dominated by the shock-associated noise source. The fourth location shown in Figure 11(d) is in the region dominated by the mixing noise source. Since the predictions from the coarser mesh are very similar to those predicted by the fine mesh, only fine mesh results are shown in these figures. The distance between LES probes and microphone locations is within 0.3D for the first two locations, and within 0.7D for the third and fourth locations. These are acceptable choices considering that the grid resolution of microphones in the measurement is roughly 0.4D, and the difference between the LES and measurement peak locations is around 1D. The overall agreement with the measurement data is very good that both the noise level and the peak location all agree well with the measurements.

Figure 12 shows instantaneous pressure distributions for both shock-containing and shock-free jets at the three jet temperatures. It can be seen that the shock-containing jet at the cold jet condition shows a large shock-associated noise source region from the nozzle exit to the location of x = 15D, which is roughly $1.5L_c$ and is near the peak location of the centerline turbulent kinetic energy as shown in Figure 8 and 9. The shock-associated acoustic waves propagate in both upstream and downstream directions, but the region after x = 15D is dominated by downstream propagating mixing waves. On the other hand, the shock-free jet has a much quieter region upstream of the end of the potential core and the noise is dominated by the mixing noise through the entire region, where the pressure waves propagate mainly in

the downstream direction. As the temperature increases, the mixing noise generation increases and Mach wave propagation dominates. On the other hand, the changes in shock-associated noise generation appear to be much smaller, and thus the shock-containing and shock-free distributions become more similar. Figure 13 shows the overall sound pressure levels along the FW-H integral surface. At the cold jet condition, both the shock-containing and shock-free distributions reach a substantial level at roughly $x = $ 2D and this substantial level extends to roughly $x = 11$D in the shock-containing jet, and $x = 15$D ($\sim 1.5 L_c$) in the shock-free jet. The difference between the shock-containing and shock-free jets is large at this cold jet condition and the difference can be observed up to $x = 15$D. The increase in the temperature elevates the overall sound pressure level, but the difference between the shock-containing and shock-free distributions becomes smaller, similar to the trend shown in the instantaneous fields in Figure 12. The beginning location with the substantial noise intensity moves closer to the nozzle exit as the jet temperature increases. Figure 14 shows SPL contour distributions along the FW-H integral surface at $T_o/T_{amb} = 1.0$ and 2.0. The heated jet condition of $T_o/T_{amb} = 3.0$ is not shown here because it presents a very similar scenario as that of $T_o/T_{amb} = 2.0$. At the shock-free cold jet condition, large scales dominate the noise generation, and the dominant noise source extends from 5D to 25D. When shock cells are present, the shock-associated broadband component is clearly observed and the peak frequency increases in the downstream direction. This trend has been reported in several measurements as shown in Refs. [10][16][17]. Seiner and Yu [10] considered this near-field shift a Doppler effect, similar to that in the far field. The dashed line shown in Figure 14(a) is the Strouhal number based on the local shock cell size, $St = \frac{U_c}{U_j} / \frac{L_s(x)}{D}$, where U_c is the convection velocity and $L_s(x)$ is the local shock-cell size, ranging from 1.4D to 0.8D. The convection velocity U_c has been considered to be around $0.7 U_j$ [2]. Since U_c does not impact the slope of the curve, which is solely determined by the local shock cell size, $U_c = 0.6 U_j$ is used to give a better match with the shock-associated broadband peak frequency location. It can be seen that the axial variation of the broad peak frequency agrees very well with this curve, indicating that the near-field variation of the broad peak frequency is dictated more by the shock-cell size variation, rather than by the Doppler effect. It is expected that this axial variation of the near-field peak frequency would also impact the variation of the far-field broadband peak frequency. In addition, the shock-associate noise distribution shows several ripples branching from the broadband peak frequency region and increasing quickly to higher frequencies. Those patterns are possibly correlated with the shock-cell structures, but details of this correlation are left for a future study.

When the total temperature is increased to $2T_{amb}$, the mixing noise contribution is greatly increased both near the nozzle exit and also at downstream locations. The shock-associated contribution is still present, but it is overshadowed by the mixing contribution. The increase of high-frequency mixing components is confined to near the nozzle exit, and the peak frequency shifts slightly to higher values when the location moves closer to the nozzle exit. This trend has also been observed in measurements shown in Refs [15][36]. On the other hand, the low-frequency increase is observed at locations downstream of around $x = 5$D. The dashed lines shown in the shock-free distributions in Figure 14(b) and (c) are the estimation of the maximum noise source location, $x/D(St) = 5.1 - 7.3 Log_{10}St$, given in Refs [15][36]. It can be seen that this formulation presents reasonably well in the heated jet, but a larger difference is observed in the cold jet. In addition, it can be clearly seen that the axial variation of the peak frequency of the shock-associated noise source presents an opposite trend to that of the mixing noise source. Figure 15 shows the quantitative measure of the jet temperature effect on the near-field shock-associated noise distributions, where SPL distributions of the three jet temperatures at 1.5D above the nozzle exit are shown. The distribution with the Strouhal number normalized by the peak frequency is also presented. This location is chosen because it is least contaminated with the mixing noise. It can be seen that a screech tone with a similar intensity is present in all profiles, and the shock-associated noise component shows a similar spectral shape if the frequency is normalized by the screech frequency. On the other hand, the heating effect increases both the low-frequency and high-frequency ($St>0.8$) components. The low-frequency peak is located between $St = 0.1$ to 0.2 and is near 60% of the screech frequency. This

low-frequency peak decreases in Strouhal number and increases in magnitude as the jet temperature increases. The high-frequency increase in the range of St > 0.8 is because of the high-frequency increase near the nozzle exit as shown in Figure 14. Figure 16 shows the impact of heating on the Strouhal number of the screech tone. It can be seen that it decreases as the jet temperature increases, and the trend compares well with Tam's theory in Ref. [11].

VI.   IMPACT OF SHOCK-CELLS AND HEATING EFFECT ON FAR-FIELD ACOUSTIC CHARACTERISTICS

Figure 17 compares far-field OASPL distributions with measurements at the distance of 47D. The nozzle diameter in measurements, however, is 0.813", smaller than the size used in simulations. It can be seen that the agreement is still very good, and the differences are within 2.5dB for all three jet temperatures. In addition, SPL distributions at two radiation angles are shown in Figure 18, where the scaling of the nozzle area is applied. It can be seen that both the shock-associated and mixing noise distributions agree well with measurements. The higher levels in the low-frequency region at the sideline angle shown in measurements could be introduced by the reflection of the downstream exhaust system. As a whole, the overall comparison between LES predictions and the measurements is very good.

Figure 19 shows several far-field SPL distributions of both shock-containing and shock-free jets at the cold and a heated jet condition. It is clear that heating reduces the overall impact of shock cells on the total noise. For example, the impact of shock-associated noise can be seen up to 140° in the cold jet, but it is only up to 120° for the heated jet. In addition, the impact of shock cells on the low-frequency range is very small, which agrees with experimental observations, for example, in Refs [13][14]. Figure 20 shows the far-field OASPL of both shock-associated and shock-free jets at three jet temperatures. It also includes differences between shock-containing and shock-free jets and also shock-associated contributions. The heating effect greatly increases the downstream noise level, especially the peak noise level, which is dominated by Mach wave radiation, but shock cells have almost no effect on this peak level. This trend is also observed in measurements, for example in Ref. [13]. The negligible effect of shock cells on the low-frequency components and also on the peak noise level indicates that shock cells do not impact the mixing noise generation and propagation. The peak angle is roughly 139.5^o at $T_o/T_{amb} = 2.0$ and 131° at $T_o/T_{amb} = 3.0$. These peak angles agrees well with those calculated from Oertel convective Mach wave number $M_c^{'}$ [33], which give 136.7^o and 131.7^o at these two heated conditions. The calculated peak angle for the cold jet condition is 150°, which is the largest far field angle examined in this paper.

On the other hand, shock cells have a much larger impact in the upstream direction, as can be seen in both Figure 19 and Figure 20(b). The noise level in the shock-containing cold jet at 40° is more than 9dB higher than that in the shock-free cold jet. But this impact is gradually reduced in the downstream direction and terminated slightly upstream of the peak radiation angle. The magnitude and the area of this impact are also reduced as the jet temperature increases. Since the difference in OASPL measures the ratio between noise levels of shock-containing and shock-free jets, it only reflects the relative importance of shock-cell impact rather than the true shock-associated noise contribution. Thus the shock-associated contributions are computed by subtracting shock-free pressure fluctuation intensities from those in shock-containing jets, and the results are shown in   Figure 20(c). It can be seen that the shock-associated contribution increases in the upstream direction and reaches a local peak near the sideline angle, but the maximum level is located at a downstream angle followed by a rapid decrease further downstream. In addition, heating reduces the shock-associated contribution in the upstream direction, but increases it in the downstream direction. The crossover point is near the sideline angle, where the heating impact is small. Thus the heating effect has an opposite impact on the shock-associated and the mixing contributions in the upstream direction. This may explain why the heating impact on the total noise of the shock-containing jets is small at highly upstream angles. Furthermore, the difference of the shock-associated contribution over the radiation angles from the upstream angles to the angle upstream of the rapid decrease is within 1dB~2dB in the cold jet and 3dB~4dB in the heated jet of $T_o/T_{amb} = 3$. Thus the

difference over the radiation angles is small, which is consistent with the well-established experimental observation that broadband shock-associated noise is omni-directional. Most of the trends observed above can be also seen in Fig. 19 of Ref. [13], except that it shows a substantial total noise increase in the upstream direction when the jet is heated to $T_o/T_{amb} = 1.8$, although the noise level remains unchanged when the jet is further heated. It appears that LES predictions show a smaller heating impact on shock-associated noise level when the amount of heating is small. Currently we are not sure what may have introduced this difference.

Figure 21 shows the heating impact on SPL distributions at upstream and the sideline angles. Heating reduces the shock-associated peak levels, but this reduction slows down as the jet is further heated. This reduction is also lower at larger polar radiation angles, consistent with the trend shown in Figure 20(c). Similarly, Kuo, McLaughlin and Morris [15] also observed a slightly reduced peak shock-associated noise level at the underexpanded jet condition. In addition, the broadband peak Strouhal number shown in Figure 21 decreases as the jet temperature increases, which is consistent with the trend of the screech Strouhal number shown in Figure 16. But Kuo, McLaughlin and Morris observed an increase of peak Strouhal number in the underexpanded jet. It is not clear to us so far what is responsible for this difference. Figure 22 shows both the total noise and shock-associated noise contributions at 60° and 90°, and the Strouhal number is normalized by the peak Strouhal number. It can be seen that the total noise profiles collapse well with the peak Strouhal number except that the shape around the peak is getting wider as the jet temperature increases, and this trend is more prominent at 90°. When the mixing noise contribution is taken out, the shock-associated profiles remain similar as the jet temperature increases, which is consistent with the observation made by Viswanathan, Alkislar and Czech [13]. Therefore, the noise increase in both low- and high-frequency ranges in the total noise distributions is caused by the mixing noise contribution, which increases with the jet temperature and with the polar radiation angle.

Figure 23 shows SPL contour distributions for both shock-containing and shock-free jets for the cold and a heated jets. These distributions show clearly, again, that the shock-associated broadband components dominate the upstream angles, and the heating effect reduces the difference between the shock-containing and shock-free jet conditions. In addition, the broadband peak frequency shows a similar trend as that observed in the near field in Figure 14 that the change of the peak frequency slope is slow in the upstream direction, but the slope increases quickly near the end of the shock-associated broadband noise region. This fast increase region is the peak location of the shock-associated contribution shown in Figure 20. The dashed lines shown in Figure 23(a) and Figure 23(c) are the predictions from the broadband peak frequency model, $St = \frac{U_c}{U_j} / \frac{L_s}{D} / (1 + M_c cos\theta)$, proposed by Harper-Bourne and Fisher [1] and by Tam and Tanna [2]. The convection velocity was set at $0.7U_j$ and the shock cell size $L_s = 1.17D$ to match the peak Strouhal number at 90° in the cold jet. The agreement between the model and LES predictions is very good up to 130° in the cold jet and good up to 120° in the heated jet. But the model under-predicts the rapid increase near the end of shock-associated noise region. Since the shock-associated noise source is distributed along the jet core, as shown in Figure 14, the radiation angle θ may be different for each shock cell if the observer's location is not at a sufficient distance. Kuo, Veltin and McLaughlin [37] have shown that a significant far-field distance is needed to obtain a true geometric far field. In other words, if the far field is not far enough, the noise source cannot be considered as a point source and the distributed nature of the source could impact the far-field noise characteristics. Therefore, to see if the term of $(1 + M_c cos\theta)$ is responsible for the difference shown in the rapid increase region, the noise level of the cold jet at a much larger distance of 1000D is computed and the shock-associated peak frequency along with that of 47D are shown in Figure 24. The peak frequency is found higher than that of the nearer location, and thus a smaller shock-cell size, $L_s = 0.97D$, is used to match the peak frequency at 90° at this larger location. It can be seen that model predictions agree well again with LES prediction up to 130° at the second far-field location. It appears that the term $(1 + M_c cos\theta)$ itself may not be the cause directly responsible for the difference shown in the region with the rapid increase of the broadband peak frequency. The axial variation observed in the shock-cell size near the end of the jet core and the variation

of the acoustic wave magnitude are more likely responsible for the fast increased slope shown in these figures. However, since the peak frequency of the shock-associated noise source varies with the axial location, the distributed shock-associated noise source may still impact the far-field noise characteristics and the change of the peak frequency with the far-field distance could be introduced by this impact. The broadband peak frequency of the shock-associated noise versus the far-field distance at the sideline angle is presented in Figure 25. It is clear that there is an initial large increase when the far-field distance is small, but the peak frequency asymptotically reaches a saturated value as the far-field distance increases beyond roughly 200D. In addition, the peak level of the shock-associated noise also varies with the far-field distance when this distance is not sufficiently large, as shown in Figure 26, where the peak levels versus the far-field distance at three radiation angles are presented and all noise levels are scaled to the level at r = 47D with the scaling law of $1/r$. It can be seen that the change at the upstream angle is small, but the change increases as the radiation angle moves to the downstream direction. The peak levels at 90° and 130° are being reduced when the far-field distance increases up to 300D. A similar trend was also observed in Ref. [13], for example in Figs 32, 33 and 35 of that paper, in which the peak frequency at 90° is slightly increased and the peak level is reduced as the far-field distance is increased from 73D to 122D. The spectrum profiles are examined in Figure 27, where SPL profiles at three far-field distances and three radiation angles are shown. Both the total noise and the shock-associated contribution are presented. It appears that increasing the far-field distance increases the low-frequency components at all radiation angles, but the change in the shock-associated high-frequency components depends on the radiation direction. The level of the shock-associated high-frequency components increases in the upstream direction, but decreases at the downstream direction. This different trend is not caused by the mixing noise contribution because the shock-associated noise distributions shown in Figure 27 also present a similar trend. Again these two different trends can be also seen in Ref. [13] from the results at 90° and 130° shown in its Fig. 32. In addition, the change of peak frequency and the noise level as the far-field distance increases is also shown in Ref. [37], but the peak frequencies and noise levels reported there are associated with the mixing noise because fully expanded jets were used in the measurements. The results reported in that paper show that the peak frequency decreases and the peak level increases as the far-field distance increases, which are similar to the trend associated with the low-frequency mixing noise component at 130° as shown in Figure 27. Furthermore, the results at r = 200D are very similar to those at r = 1000D, but it is found that results at r = 100D (not shown here) still include some impact of the far-field distance. Thus the far-field distance beyond 200D can be considered as a true geometric far-field distance for the shock-associated noise at this nozzle pressure ratio. At last it should also be mentioned that the current far-field prediction assumes a linear acoustic propagation, so the impact of the far-field distance has no contribution from non-linear effects, which are likely to further complicate the impact of the far-field distance on the noise characteristics.

Contrary to the shock-associated contribution, which presents similar patterns in both the near and the far field, the mixing noise distribution shows very different near- and far-field distributions, as shown in Figure 14 and Figure 23. This is because of the difference in the preferred propagation direction; i.e., the shock-associated noise is more omnidirectional, while the mixing noise propagates mainly downstream and most of the acoustic energy of the mixing component propagates at a narrow range of angles, aligned with the Mach wave propagation direction. In addition, the increase in the peak mixing noise level by heating shown in Figure 23 is not only found at low frequencies (large scales), but also at high frequencies (fine scales). If we examine the near-field distributions shown in Figure 14, the increase of fine-scale noise level is confined to the vicinity of the nozzle exit, but large scales are located more at downstream locations. However, both energetic fine and large scales at the heated jet condition are agglomerated around the peak radiation angle in the far field as shown in Figure 23. Thus it appears that the propagation direction of energetic fine scales introduced by heating is not omnidirectional, but rather they have a dominant downstream radiation direction, similar to that of the large-scales.

VII. CONCLUSIONS

Shock-associated noise characteristics have been investigated using large-eddy simulations. The jet condition is under-expanded, and the shock-associated noise characteristics at three jet total temperatures are investigated. To better sort out the shock-associated noise contribution, shock-free jet flows with the same fully expanded conditions are also simulated. The LES predictions have been compared with experimental data on the shock structure, jet core length, and near- and far-field noise distributions. Very good agreement has been observed overall. In addition, the power density spectral distributions of the axial velocity included an inertial range with a slope of -5/3 at all axial locations, and this pattern shifts to lower frequency in the downstream direction.

It is found that the shock cells have little impact on the jet potential core length at this under-expanded jet condition, but the heating effect reduces the jet potential core length and increases the initial shear layer spreading. Heating effect, however, has little impact on the shock-cell structure near the nozzle exit. The shock cells slightly increase the turbulence kinetic energy at the centerline, but the impact on the lip line is small except for the region near the nozzle exit. The impact of the heating effect on the turbulence kinetic energy follows the impact on the initial shear layer spreading and the jet core length, because axial profiles collapse well with the jet core length in the region downstream of initial shear layer spreading.

The impact of shock-associated noise can be seen up to roughly one and half the jet core lengths in the near field, and the broadband peak frequencies move to higher values in the downstream direction in both the near and far field. In the near field, the variation of the peak frequency matches well with the inverse of the shock-cell size, indicating that the variation of the shock-cell size, rather than the Doppler effect, is largely responsible for the near-field peak frequency shift. In the far field, the variation of the shock-associated peak frequency agrees well with the model obtained by Harper-Bourne and Fisher [1] and also by Tam and Tanna [2] over a large range of radiation angle, but the model under-predicts the fast increase near the end of the shock-associated noise region. In addition, it is found that shock cells have very small impact on the low-frequency components and also on the peak mixing noise level, indicating that shock cells do not impact the mixing noise generation and propagation. It is found that the distributed nature of the shock-associated noise source impacts the far-field noise characteristics. For example, if the far-field distance is smaller than 200D~300D, the peak frequency of the shock-associated noise increases with the far-field distance, and the peak levels at the sideline and the shallow radiation angles decrease as the far-field distance increases.

Heating reduces the difference between the shock-containing jets and the shock-free jets in both the near- and far-field, because it greatly increases the mixing noise contribution, but has much less impact on the shock-associated contribution. Heating decreases the shock-associated noise region in the far field, and also slightly reduces the shock-associated noise level and the peak Strouhal number in the upstream direction, but the heating impact on the shock-associated noise contribution is small near the sideline direction. In the downstream direction, heating slightly increases the shock-associated contribution, but this contribution is rapidly decreased slightly upstream the peak radiation angle. The LES prediction of the heating impact on screech frequency agrees well with Tam's theory [11]. In addition, the heating impact on the spectral shape of the shock-associated profile is small in both the near and far field. Furthermore, the increase of the mixing noise at the peak radiation angle is found not only in the low frequencies, but also at the high frequencies. In the near field, the high-frequency increase is confined to near the nozzle exit. It appears that energetic fine scales elevated by heating also propagate near the peak radiation direction.

ACKNOWLEDGEMENTS

REFERENCES

[1] Harper-Bourne, M., and Fisher, M. J., "The Noise from Shock Waves in Supersonic Jets," AGARD-CP-131, 1973, pp. 1-13.

[2] Tam, C. K. W., and Tanna, H. K., "Shock Associated Noise of Supersonic Jets from Convergent-Divergent Nozzles," Journal of Sound and Vibration, 81(3), 1982, pp. 337-358.

[3] Tanna, H. K., "An Experimental Study of Jet Noise. Part II: Shock Associated Noise," Journal of Sound and Vibration, 50(3), 1977, pp. 429-444.

[4] Tam, C. K. W., "Stochastic Model Theory of Broadband Shock Associated Noise from Supersonic Jets," Journal of Sound and Vibration, 116(2), 1987, pp. 265-302

[5] Seiner, J. M., and Norum, T. D., "Experiments on Shock Associated Noise of Supersonic Jets," AIAA paper 79-1526, 1979.

[6] Seiner, J. M., and Norum, T. D., "Aerodynamic Aspects of Shock Containing Jet Plumes," AIAA paper 80-0965, 1980.

[7] Norum, T. D., and Seiner, J. M., "Measurements of Static Pressure and Far Field Acoustics of Shock-containing Supersonic Jets," NASA TM 84521, 1982.

[8] Norum, T. D., and Seiner, J. M., "Broadband Shock Noise from Supersonic Jets," AIAA Journal, Volume 20, No. 1, 1982, pp. 68-73.

[9] Seiner, J. M., "Advances in High Speed Jet Aeroacoustics," AIAA paper 84-2275, 1984.

[10] Seiner, J. M., and Yu, J. C., "Acoustic Near-Field Properties Associated with Broadband Shock Noise," AIAA Journal, Volume 22, No. 9, 1984, pp. 1207-1215

[11] Tam, C. K. W., "Jet Noise Generated by Large-Scale Coherent Motion," Aeroacoustics of Flight Vehicles: Theory and Practice, Volume 1: Noise Sources, ed. H. H. Hubbard, NASA RP-1258, 1991, pp. 311-390.

[12] Morris, P., and Miller, S. A. E., "Prediction of Broadband Shock-Associated Noise Using Reynolds-Averaged Navier–Stokes Computational Fluid Dynamics", AIAA Journal, Vol. 48, No. 12, December 2010.

[13] Viswanathan, K., Alkislar, M.B., and Czech, M.J., " Characteristics of the Shock Noise Component of Jet Noise", AIAA 2008-2835

[14] Tam, C. K. W., Golebiowski, M., and Seiner, J. M., **"On the Two Components of Turbulent Mixing Noise from Supersonic Jets,"** AIAA Paper 96-1716, 1996.

[15] Kuo, C-W, McLaughlin, D.K., Morris, P., "Effects of supersonic jet conditions on broadband shock-associated noise", AIAA 2011-1032.

[16] Andre, B., Castelain, T., and Bailly, C., "Broadband Shock-Associated Noise in Screeching and Non-Screeching Underexpanded Supersonic Jets", AIAA Journal, Vol. 51, No. 3 (2013), pp. 665-673.

[17] Savarese, A., P., Jordan, S, Girard, A., Royer, C., Fourment, E., Collin, Y. Gervais, and M., Porta, "Experimental study of shock-cell noise in underexpanded supersonic jets", AIAA 2013-2080.

[18] Bridges, J. and Wernet, M., "Turbulence Associated with Broadband Shock Noise in Heated Jets", AIAA-2008-2835

[19]   Veltin, J., "On the Characterization of Noise Sources Supersonic Shock Containing Jets", PhD dissertation, 2005, the Pennsylvania State University.

[20]   Munday, D., Gutmark. E., Liu, J., and Kailasanath, K. (2011), Flow structure and acoustics of supersonic jets from conic convergent-divergent nozzles, Physics of Fluids, Vol. 23, No. 11, Nov 2011, pp. 116102-1 - 116102-13.

[21]   Bodony, D.J., Ryu, J., and Lele, S.K., "Investigating Broadband Shock-Associated Noise of Axisymmetric Jets Using Large Eddy Simulation", AIAA 2006-2495

[22]   Grinstein, F.F. and Fureby, C., "On Monotonically Integrated Large Eddy Simulation of Turbulent Flows Based on FCT Algorithms", Chapter 3 in Flux-Corrected Transport: Principles, Algorithms, and Applications , Eds., D. Kuzmin, R. Löhner, and S. Turek, Springer, pp. 79-104., 2005

[23]   Lyrintzis, A., "Surface integral methods in computational aeroacoustics—From the (CFD) near-field to the (Acoustic) far-field", International Journal of Aeroacoustics, Volume 2, Number 2 / April 2003, pp. 95-128

[24]   Löhner, R., Morgan, K., Peraire, J., and Vahdati, M., "Finite element flux-corrected transport (FEM-FCT) for the Euler and Navier- Stokes equations," International Journal for Numerical Methods in Fluids, Vol. 7, No. 10, 1987, pp. 1093–1109.

[25]   Löhner, R., Applied CFD Techniques, J. Wiley & Sons, 2008.

[26]   Kuzmin, D., Möller, M., and Gurris, M., "Algebraic Flux Correction II: Compressible Flow Problems," in Flux-Corrected Transport: Principles, Algorithms, and Applications , Eds., D. Kuzmin, R. Löhner, and S. Turek, Springer, pp. 193–238., 2012

[27]   Boris, J.P., and Book, D.L., "Flux-corrected Transport I:SHASTA a fluid transport algorithm that works", Journal of Computational Physics, Volume 11. Issue 1. Pages: 38-69 (1973)

[28]   Luo, H., Baum, J., and Löhner, R., "Edge-Based Finite Element Scheme for the Euler Equations, AIAA Journal, Vol. 32, No. 6, 1994, pp.1183–1190.

[29]   Zalesak, S.T., "Fully multidimensional flux-corrected transport algorithms for fluids", Journal of Computational Physics, Vol. 31, No. 3, 1979, pp. 335–362.

[30]   Liu, Junhui; Kailasanath, K.; Ramamurti, Ravi; Munday, David; Gutmark, Ephraim; Löhner, Rainald, "Large-Eddy Simulations of a Supersonic Jet and Its Near-Field Acoustic Properties", AIAA Journal, vol. 47, issue 8, pp. 1849-1864

[31]   Shapiro, A. H., "The Dynamics and Thermodynamics of Compressible Fluid Flow", Vol. I, published by John Wiley & Sons.

[32]   Krothapalli, A., Greska, B., and Wishart, D., "Aeroacoustics of a Heated Mach 2.0 Jet", AIAA 2005-2931.

[33]   Oertel, H., (1979), Mach wave radiation of heated supersonic jets. In Mechanics of Sound Generation in Flows (ed. E. A. Muller), pp. 275–281. Springer

[34]   Greska, B., "Supersonic jet noise and its reduction using microjet injection", PhD dissertation, 2005, the Florida State University.

[35]   Viswanathan, K., "Aeroacoustics of hot jets", *J. Fluid, Mech* (2004), vol. 516, pp. 39-82.

[36]   McLaughlin, D., Kuo, C.W., and Papamoschou, D., "Experiment of the effect of ground reflections on supersonic jet noise", AIAA 2008-22.

[37]   Kuo, C-W, Veltin, J., and McLaughlin, D.K., "Effects of jet noise source distribution on acoustic far-field measurements", International journal of Aeroacoustics volume 11, number 7&8, 2012. Pages 885-915.
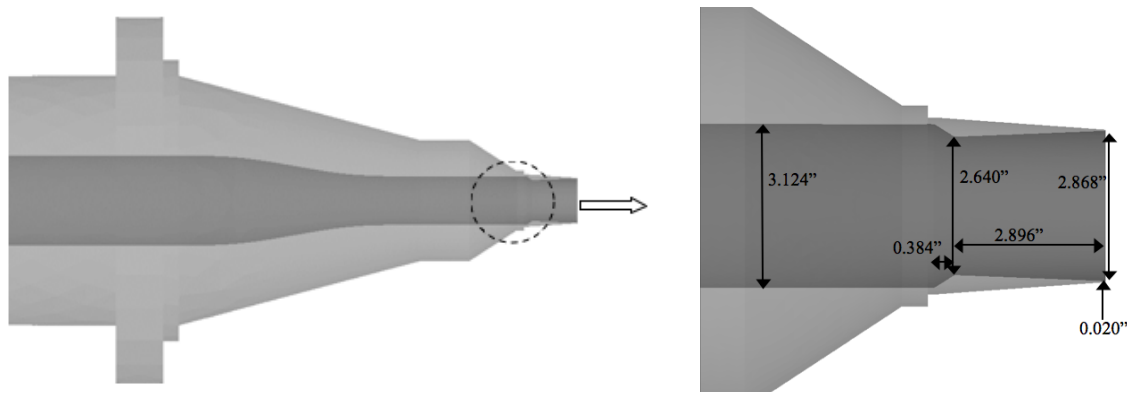
Figure 1. Nozzle geometry. The figure on the right is an enlarged version of the area near the nozzle throat and the exit.
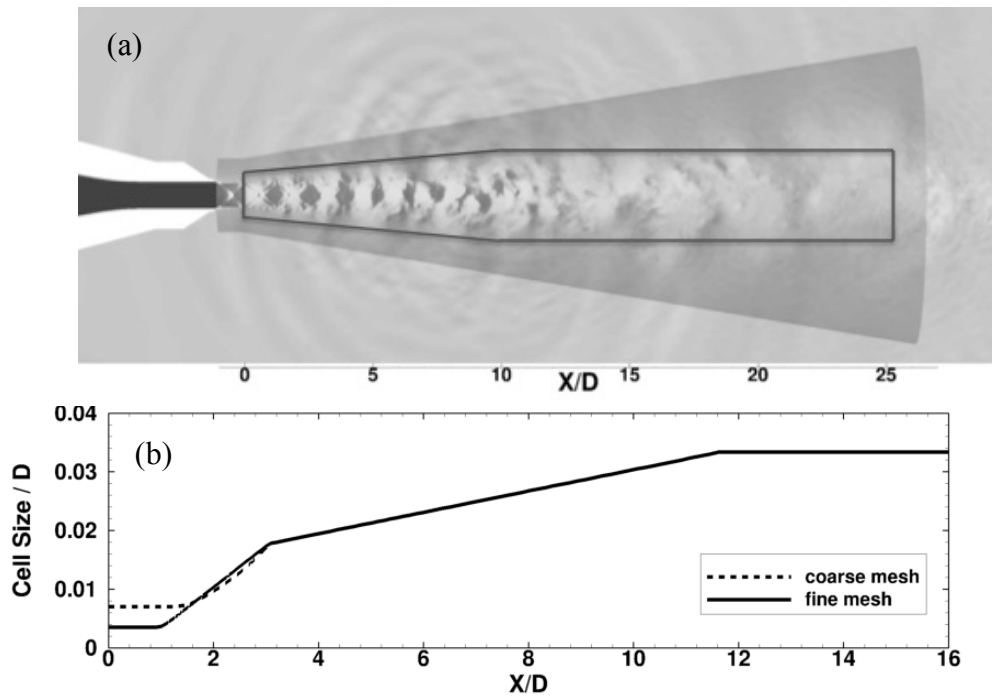
Figure 2. (a). Computational domain, where the useful near field is enclosed by the nozzle surface and the funnel-shaped surface. (b). Axial cell size distribution along the lip line. X is the axial coordinate.
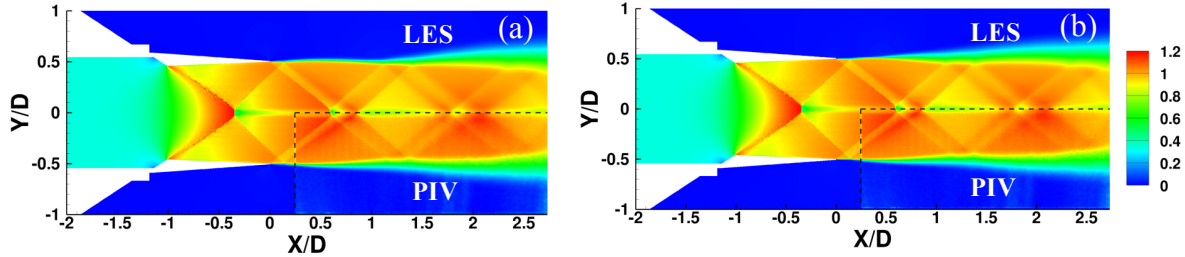
Figure 3. Comparison of shock cell structures and locations between LES prediction and PIV measurement of the baseline configuration. (a). coarser mesh prediction.(b). fine mesh prediction.
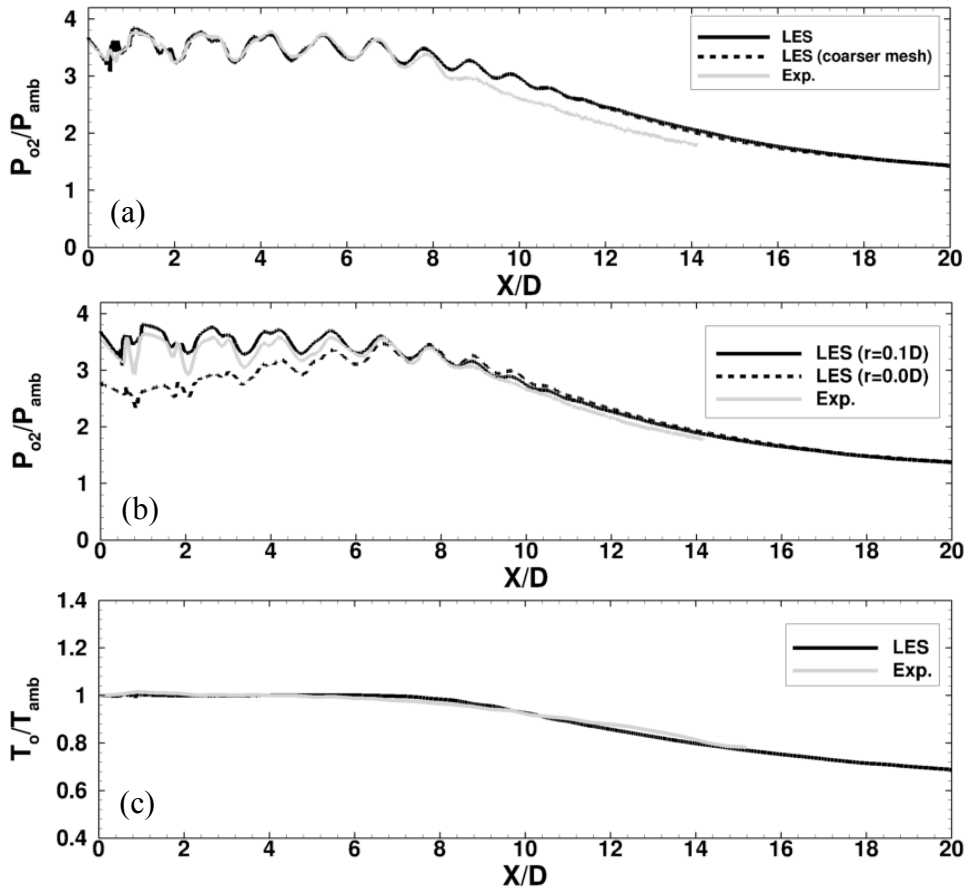
Figure 4. Comparison of jet flow quantities near the jet axis. (a). Total pressure along an axial line slightly off the jet axis by 0.1D in the cold jet. (b). Total pressure along the centerline and also along the line slightly off the jet axis at T_o/T_{amb} = 2.0. (c). Centerline total temperature at T_o/T_{amb} = 2.0. The subscript "amb" indicates ambient conditions.

$T_o/T_{amb} = 1.0$
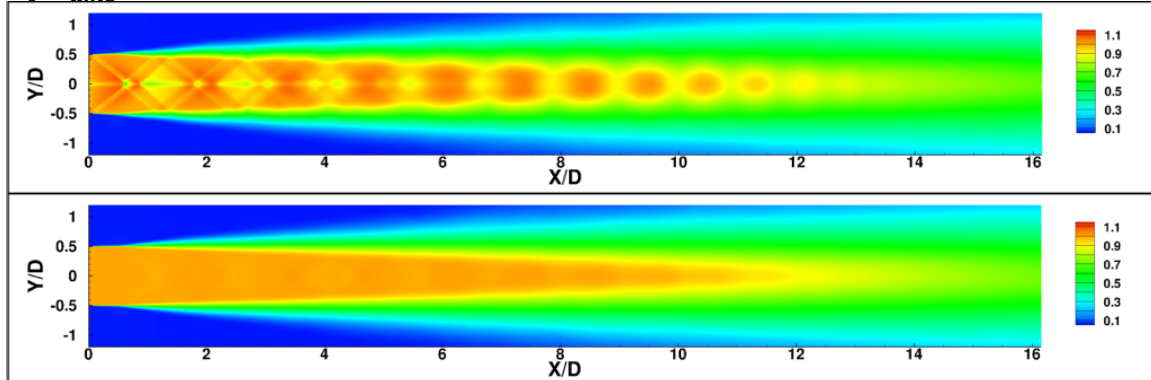
$T_o/T_{amb} = 2.0$
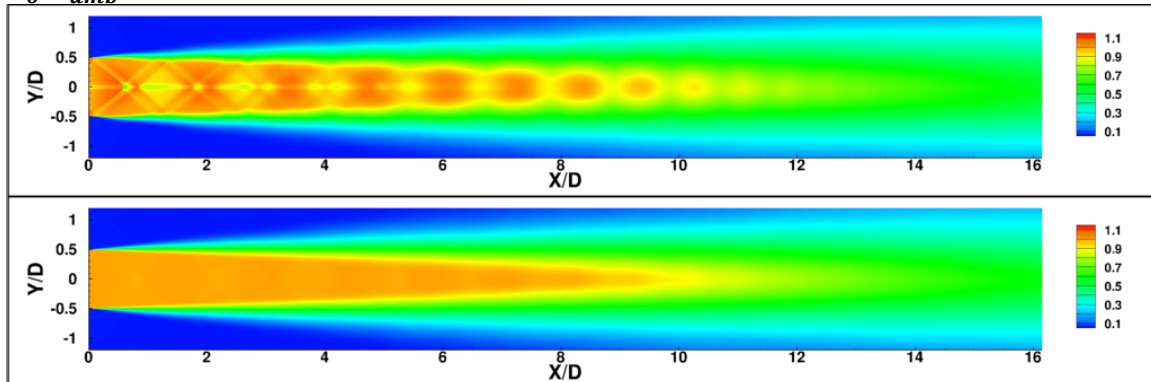
$T_o/T_{amb} = 3.0$
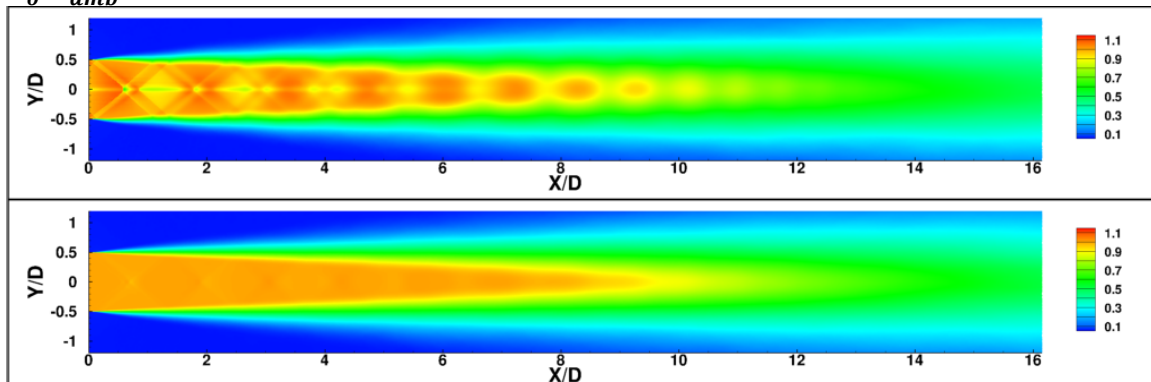
Figure 5. Time averaged streamwise velocity distributions of shock-containing jets and shock-free jets at three total temperatures. At each temperature, the top is shock-containing distribution and the bottom is the shock-free distribution.
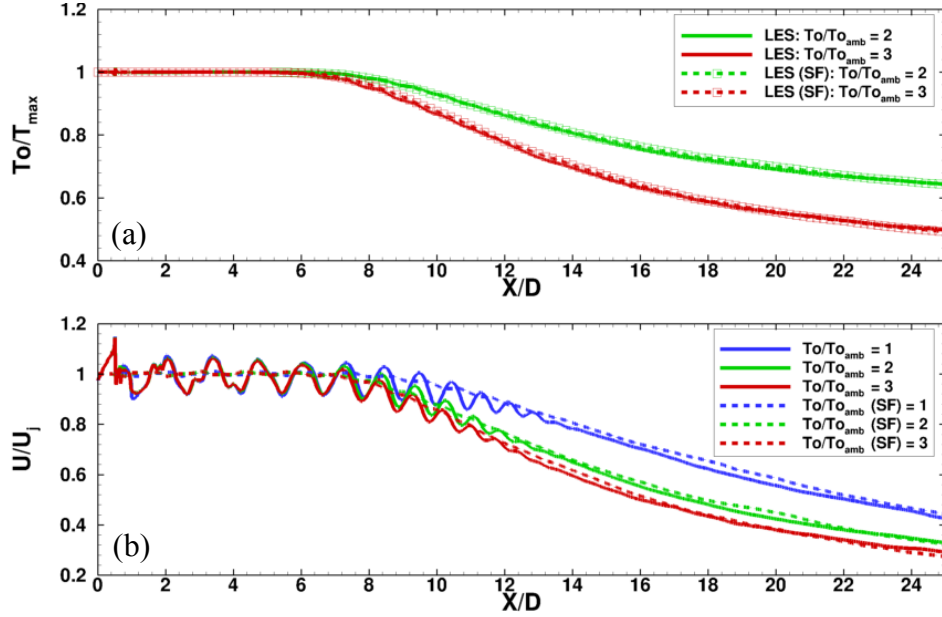
Figure 6. Centerline distributions of the total temperature and axial velocity. (a). Total temperature. (b). Axial velocity distributions at three jet total temperatures with and without shock cells. Sold lines: shock-containing jets. Dashed lines: shock-free (SF) jets.
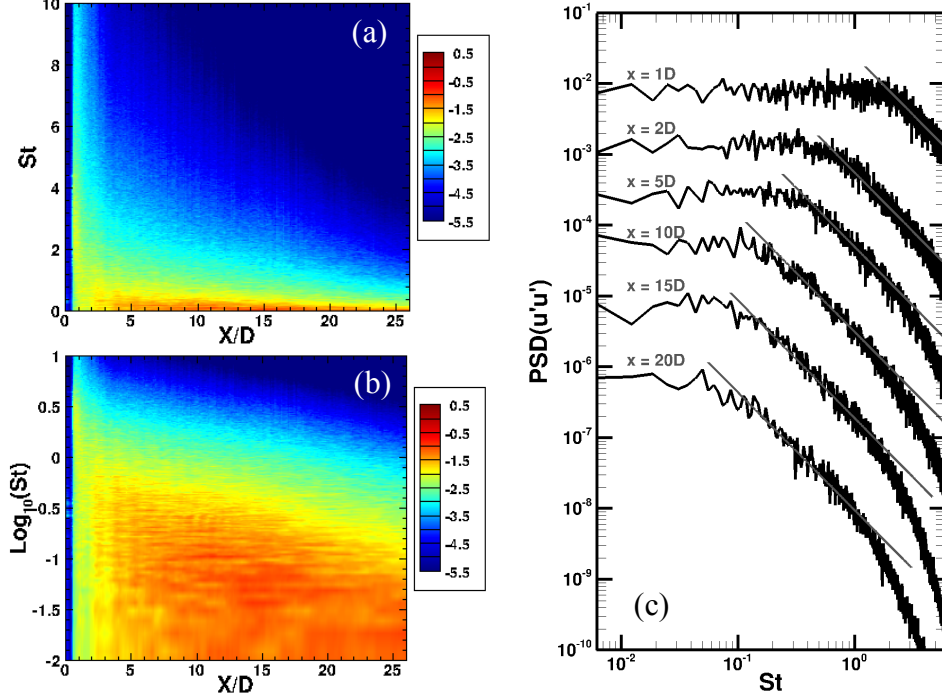
Figure 7. The power spectral density of the axial velocity in the cold shock-containing jet. (a)-(b). Distributions of $Log_{10}[PSD(u'u')]$ along the lip line. (c) PSD at several axial locations along the lip line. The magnitude is reduced by 0.1 subsequently at each location. Straight lines have a slope of -5/3.
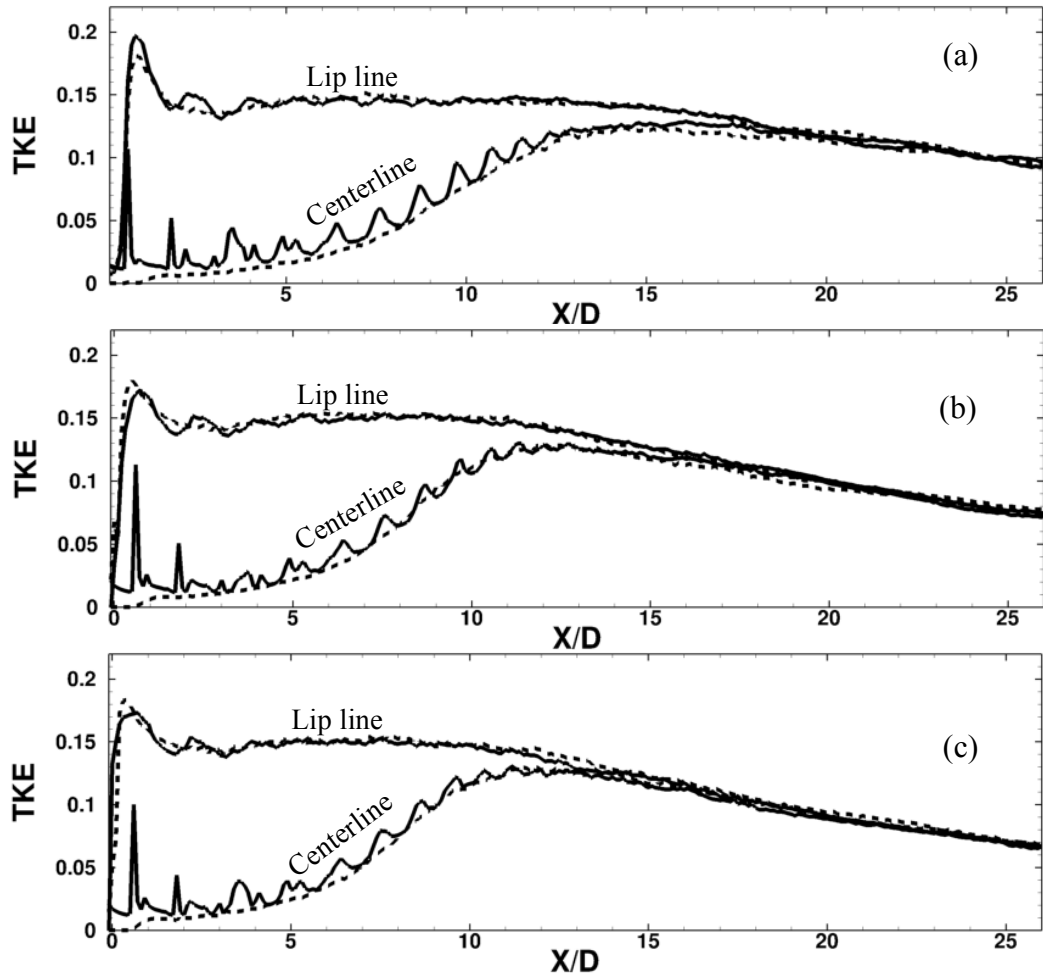
Figure 8. Turbulence kinetic energy at both the centerline and the lip line. (a). T_o/T_{amb} = 1.0 (cold jet). (b). T_o/T_{amb} = 2.0. (c). T_o/T_{amb} = 3.0. Solid lines: shock-containing jets. Dashed lines: shock-free jets.
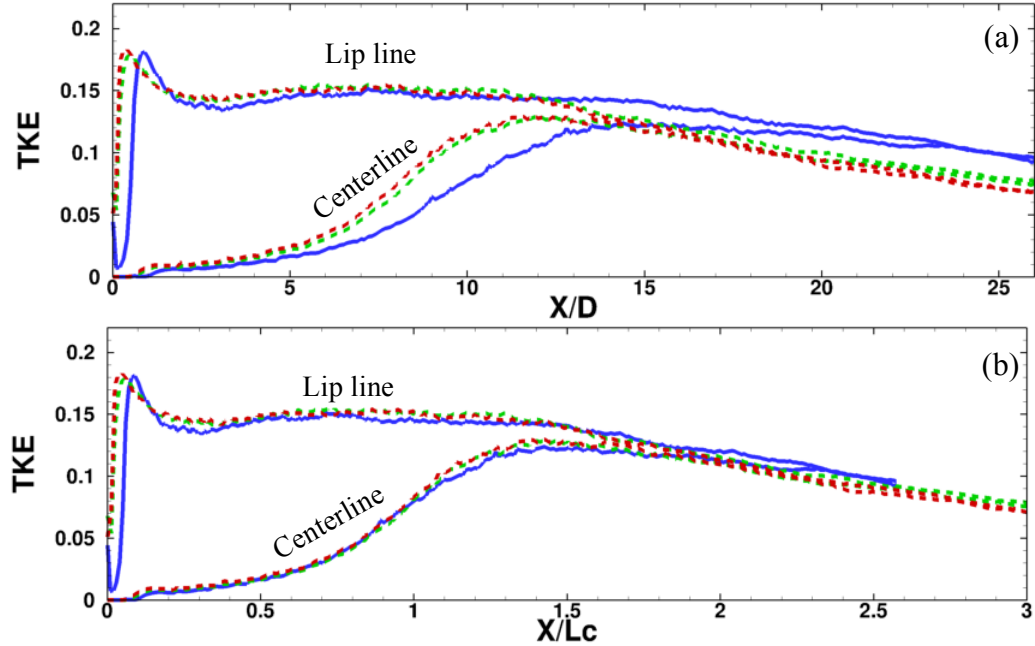
Figure 9. Turbulence kinetic energy along both the centerline and the lip line in shock free jets. Blue lines: $T_o/T_{amb} = 1.0$ (cold jet). Green lines: $T_o/T_{amb} = 2.0$. Red lines: $T_o/T_{amb} = 3.0$. (a). x axis is normalized by the nozzle exit diameter. (b). x axis is normalized by the jet potential core length Lc.
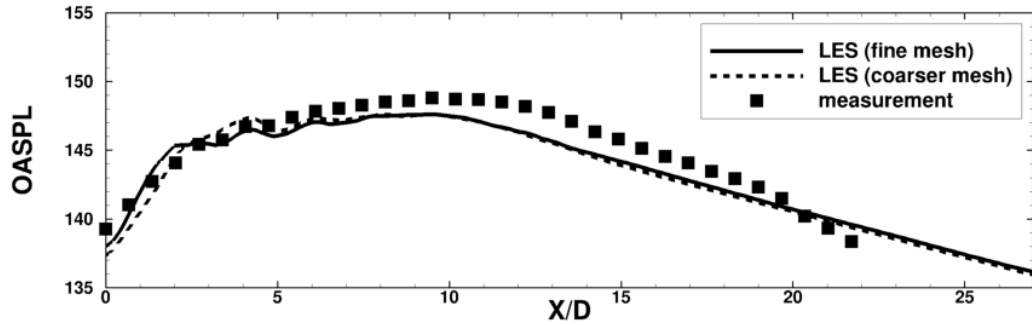
Figure 10 Distributions of the near-field overall sound pressure level along the FW-H integral surface. The data is averaged over the circumferential direction.
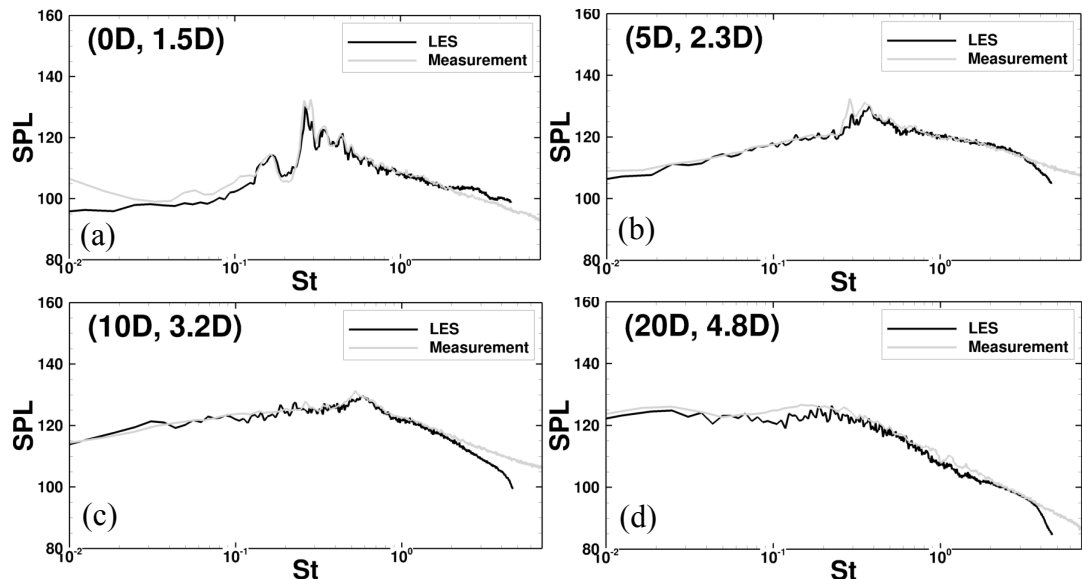
Figure 11. Spectral distributions of the near field sound pressure levels (SPL) between LES predictions and measurement data for the cold jet condition using the fine mesh. The coordinates shown are axial and radial coordinates, and the four locations are on the FW-H integral surface.
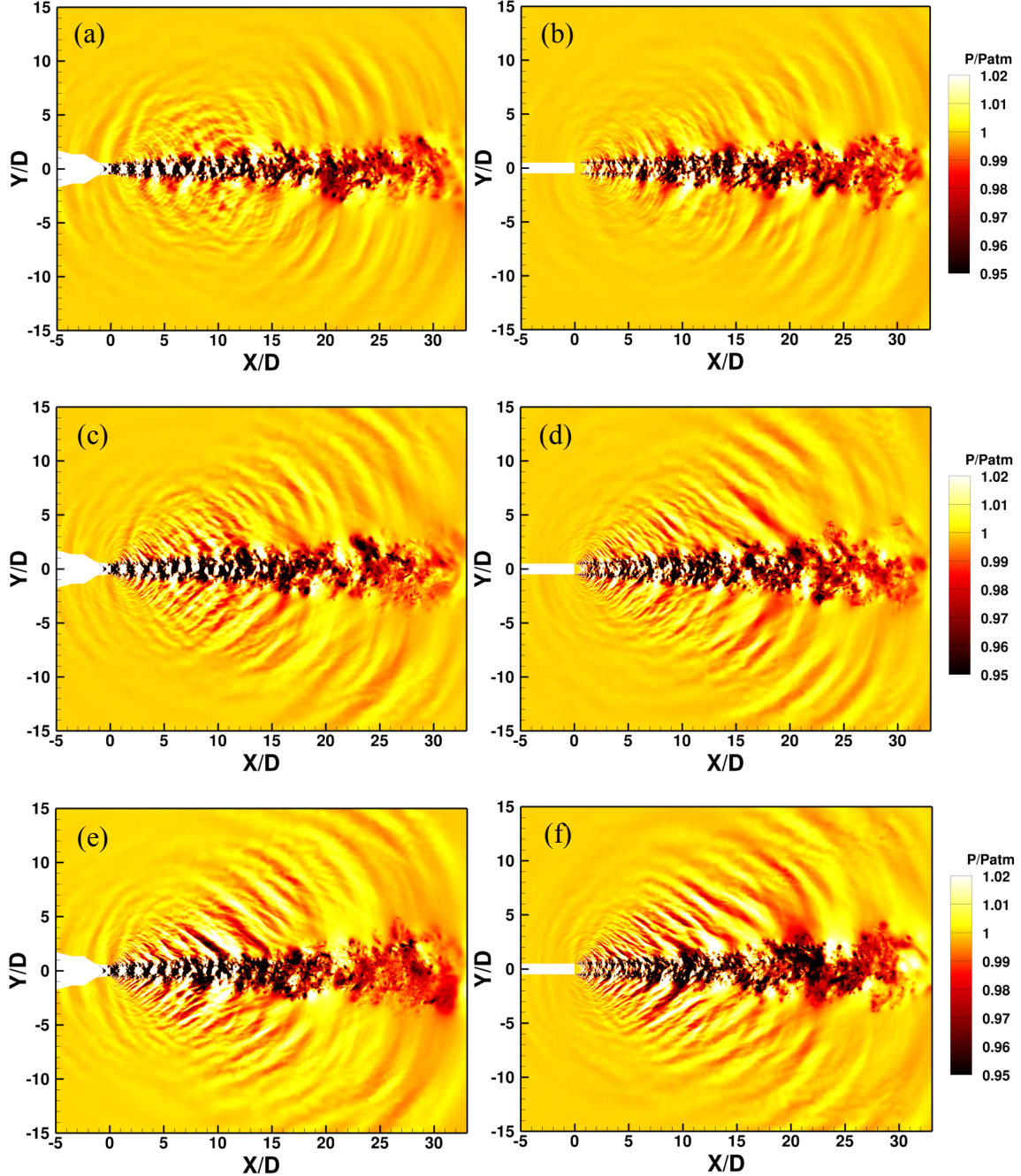
Figure 12. Instantaneous pressure distributions for both shock-containing and shock-free jet conditions. Figures on the left are shock containing; on the right are shock free. (a)-(b). T_o/T_{amb} = 1.0 (cold jet). (c)-(d). T_o/T_{amb} = 2.0. (e)-(f). T_o/T_{amb} = 3.0.
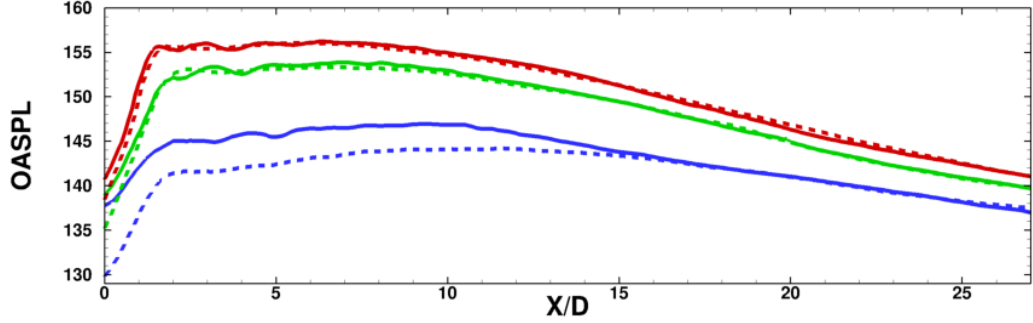
Figure 13. Overall sound pressure levels along the FW-H integral surface. Blue lines: T_o/T_{amb} = 1.0 (cold jet). Green lines: T_o/T_{amb} = 2.0. Red lines: T_o/T_{amb} = 3.0. Solid lines: shock-containing jets. Dashed lines: shock-free jets.
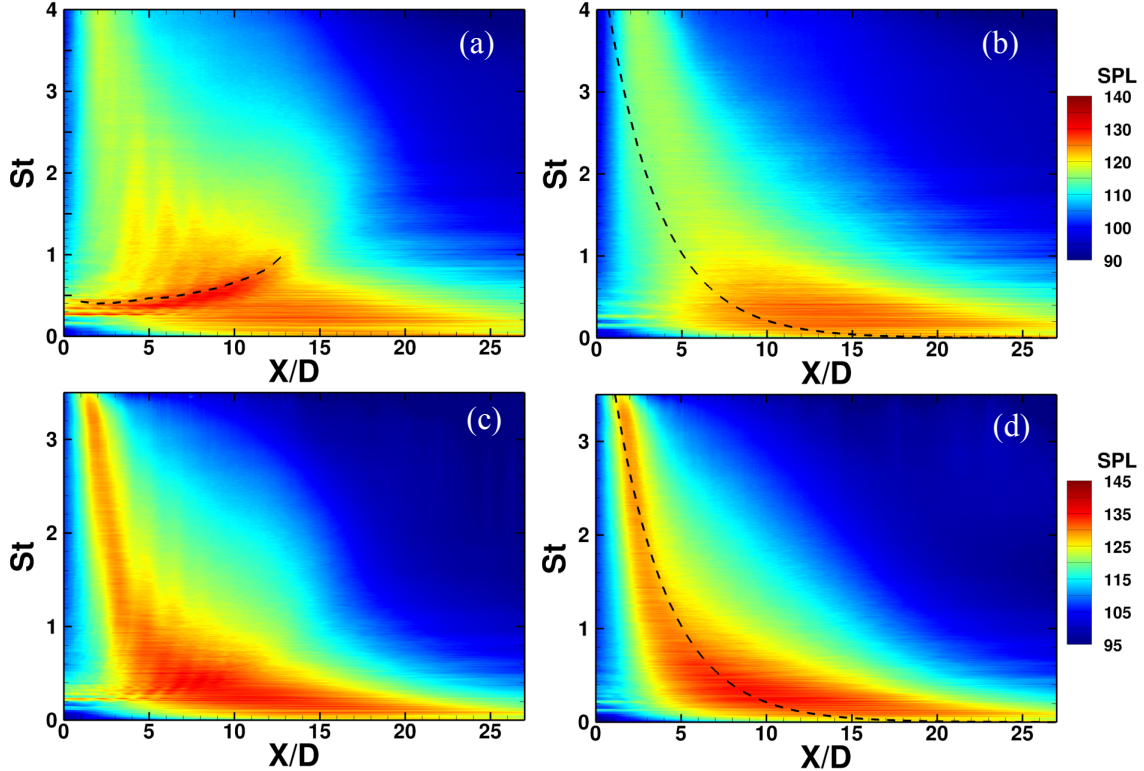
Figure 14. Sound pressure level distributions along the FW-H integral surface. (a)-(b). T_o/T_{amb} = 1.0 (cold jet). (c)-(d). T_o/T_{amb} = 2.0. Figures on the left are shock containing, and on the right are shock free. The dashed line in (a) is the axial variation of Strouhal number based on the local shock-cell size. The dashed lines in (b) and (d) are the estimation of the maximum noise source location, $x/D(St) = 5.1 - 7.3 Log_{10}St,$ from Refs [15][36].
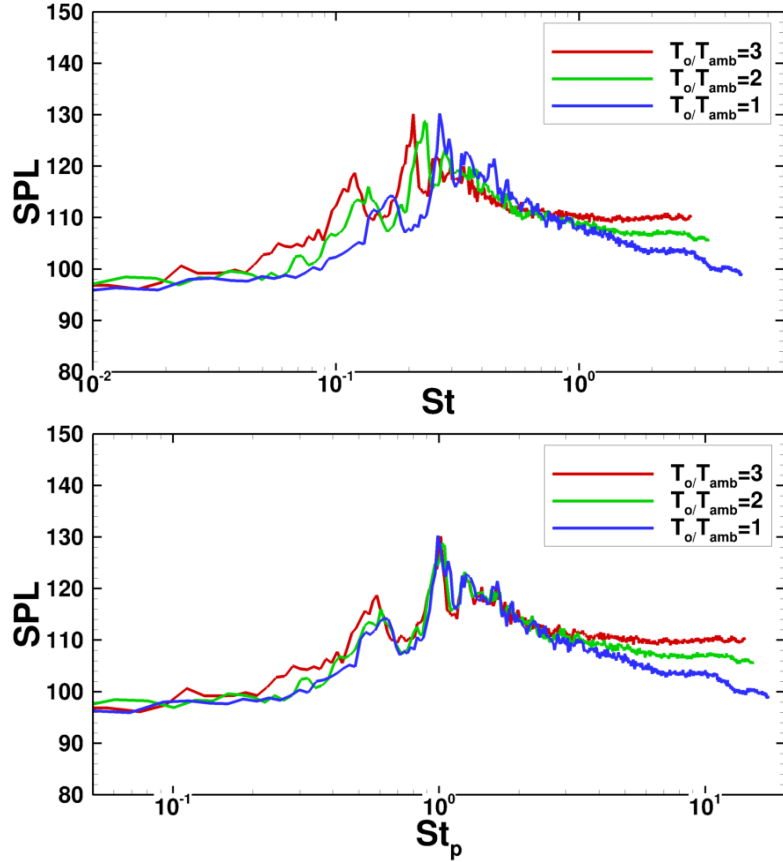
Figure 15. Sound pressure level distributions at 1.5D above the nozzle exit at three jet temperature conditions. The Strouhal number in the lower figure is normalized with the screech Strouhal number.
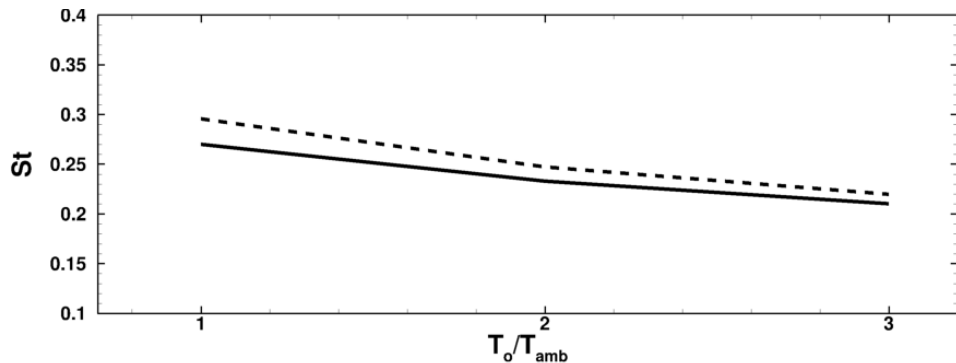
Figure 16. Jet temperature effect on the screech Strouhal number. Solid line: LES. Dashed Line: Tam's model in Ref. [11].
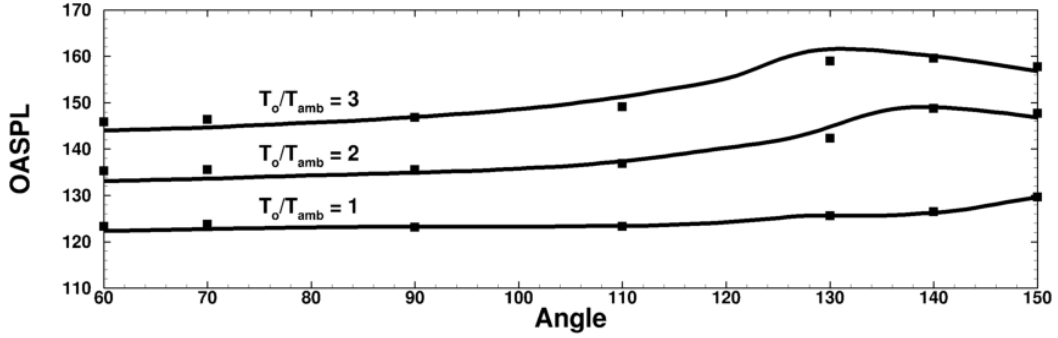
Figure 17. Far-field overall sound pressure level, OASPL $+ (T_o/T_{amb} - 1) * 10$. The coordinate of the angle is from upstream to the downstream directions. Lines: LES. Symbols: measurements.
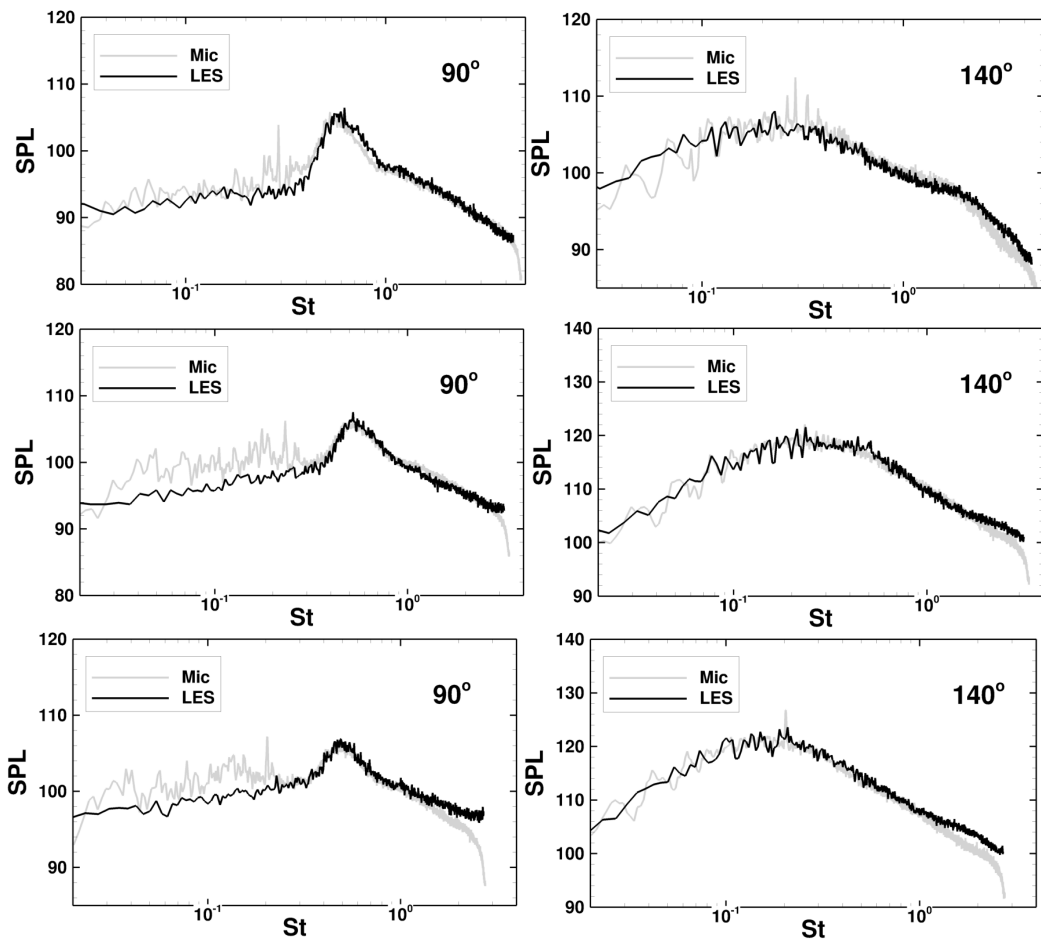
Figure 18. SPL distributions at three jet temperatures. Top figures: $T_o/T_{amb} = 1$. Middle figures: $T_o/T_{amb} = 2$. Bottom figures: $T_o/T_{amb} = 3$. Black lines: LES results. Grey lines: measurements.
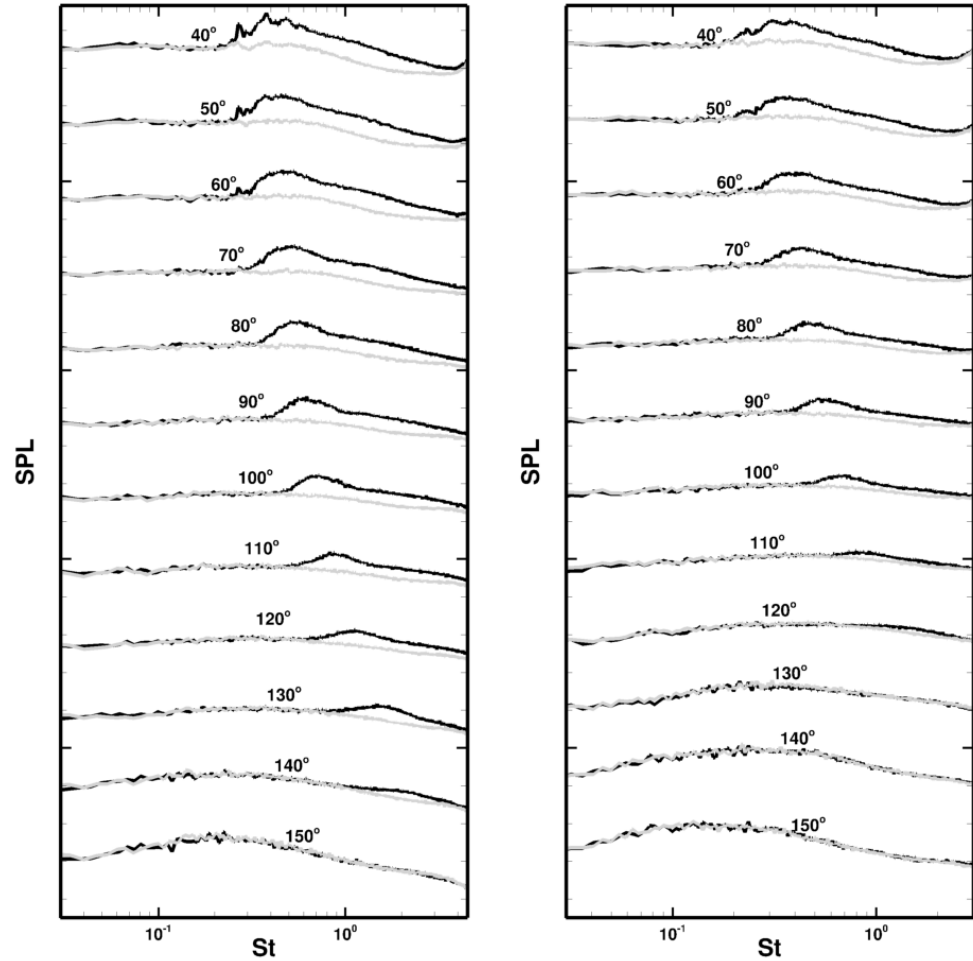
Figure 19. Far field sound pressure level distributions at the jet conditions of T_o/T_{amb} = 1.0 (left) and T_o/T_{amb} = 2.0 (right). Dark lines: shock-containing jets. Gray lines: shock-free jets.
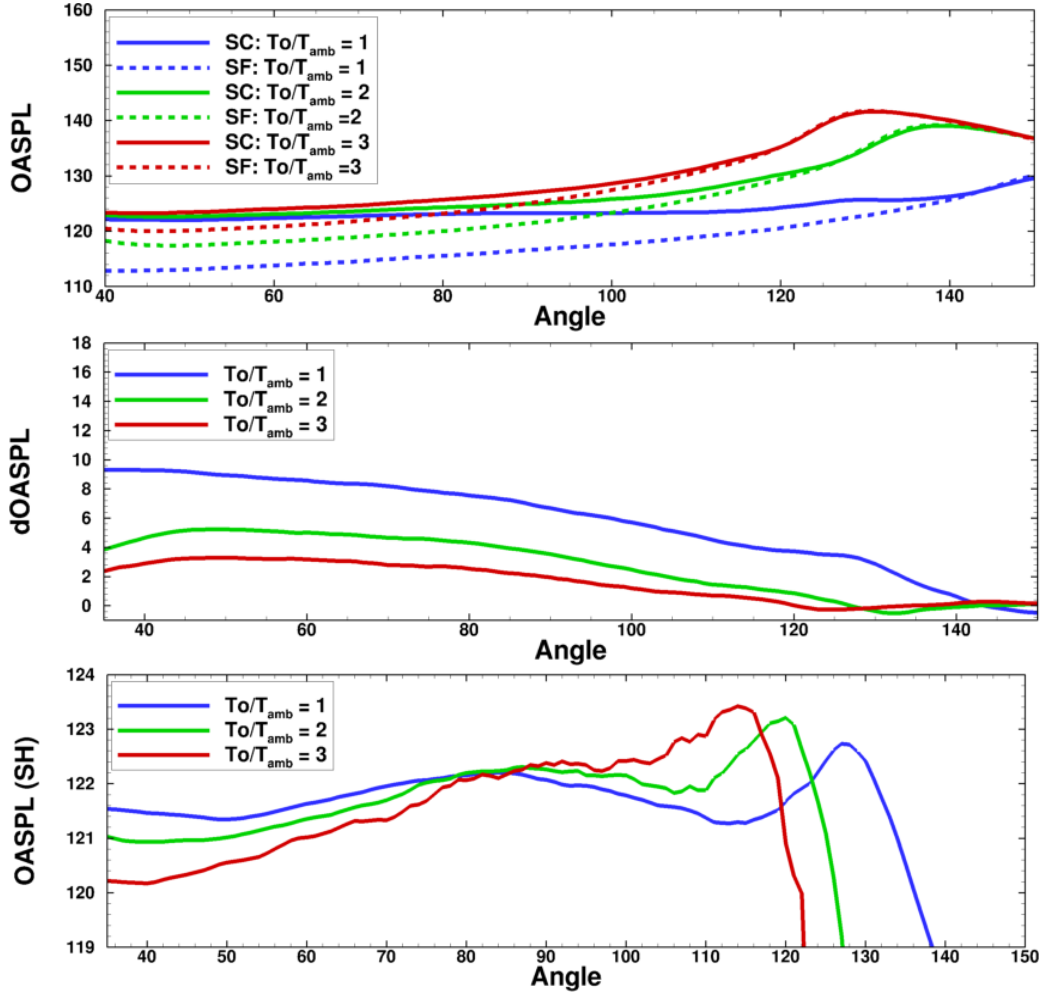
Figure 20. Far field distributions associated with OASPL. (a). Total noise. Solid lines: shock-containing (SC) jets. Dashed lines: shock-free (SF) jets. (b). Differences between shock-containing and shock-free noise levels. (c). Shock-associated contributions.
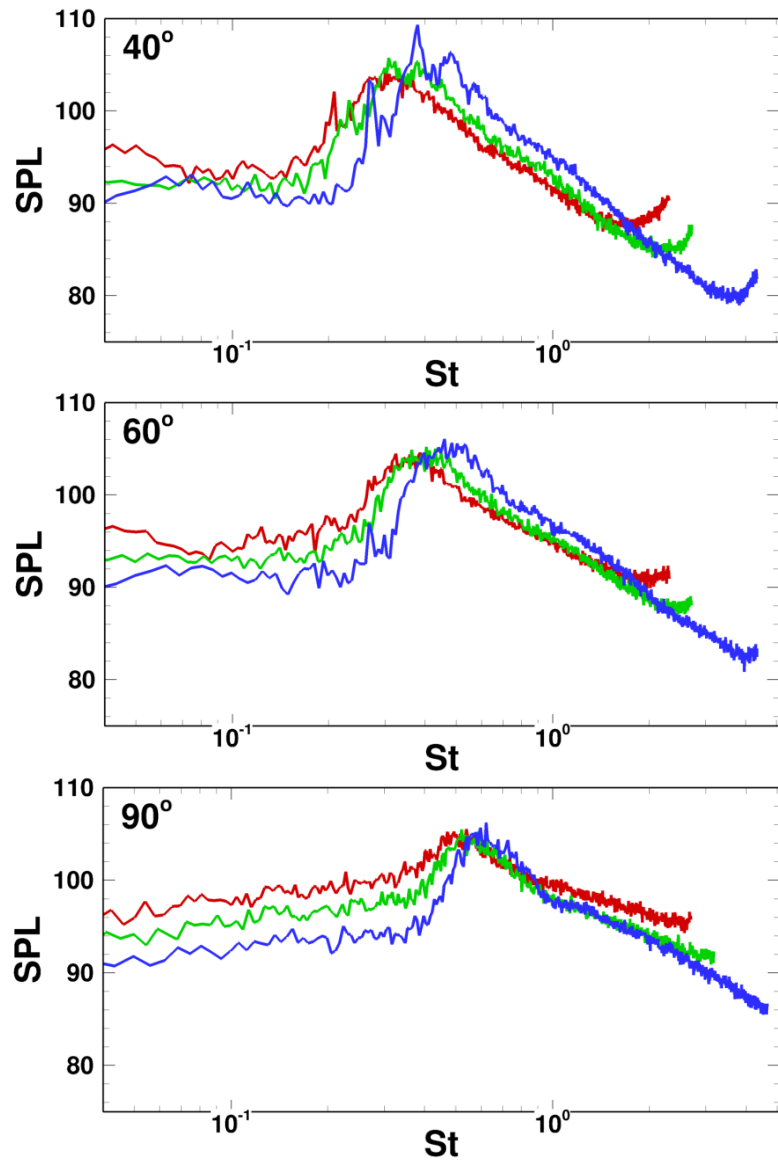
Figure 21. Far field sound pressure level spectral distributions of the shock-containing jets with $T_o/T_{amb} = 1.0$ (blue lines), 2.0 (green lines), and 3.0 (red lines).
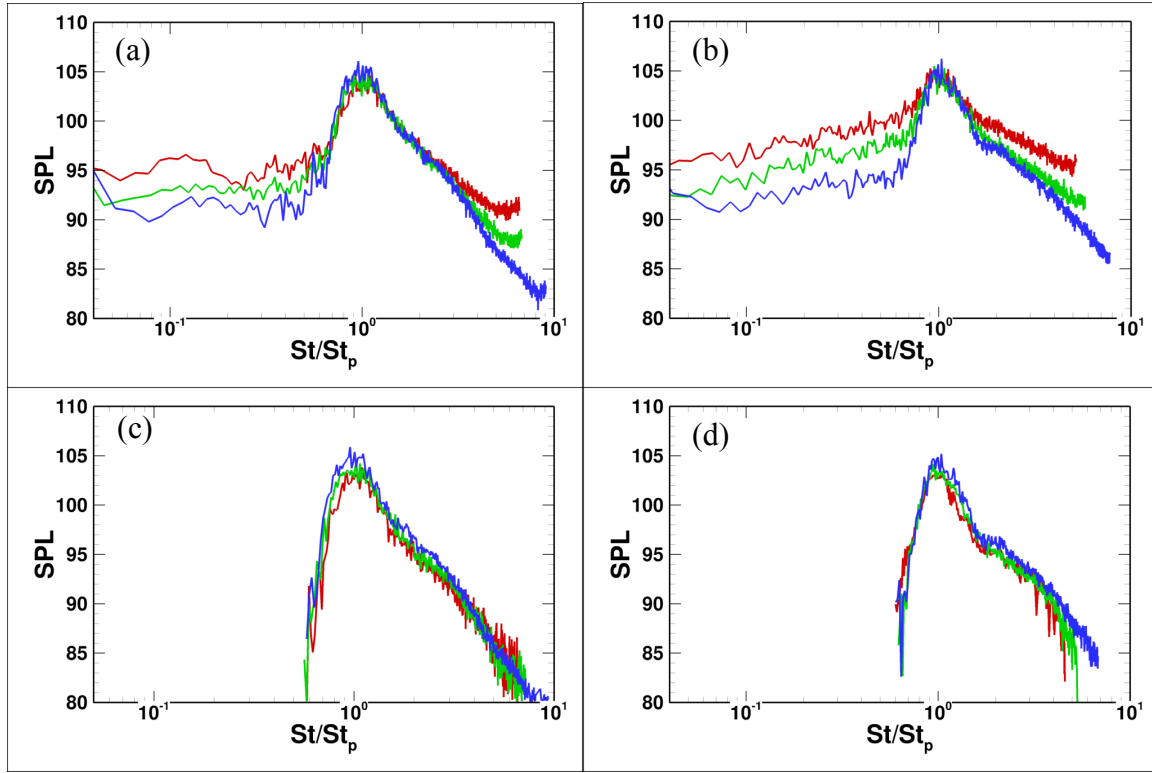
Figure 22. Heating impact on shock-associated noise profile with T_o/T_{amb} = 1.0 (blue lines), 2.0 (green lines), and 3.0 (red lines). Strouhal number is normalized by the peak Strouhal number (St_p). Left figures are at 60°, and right figures are at 90°. (a)-(b). Total noise distributions. (c)-(d) Shock-associated noise contributions.
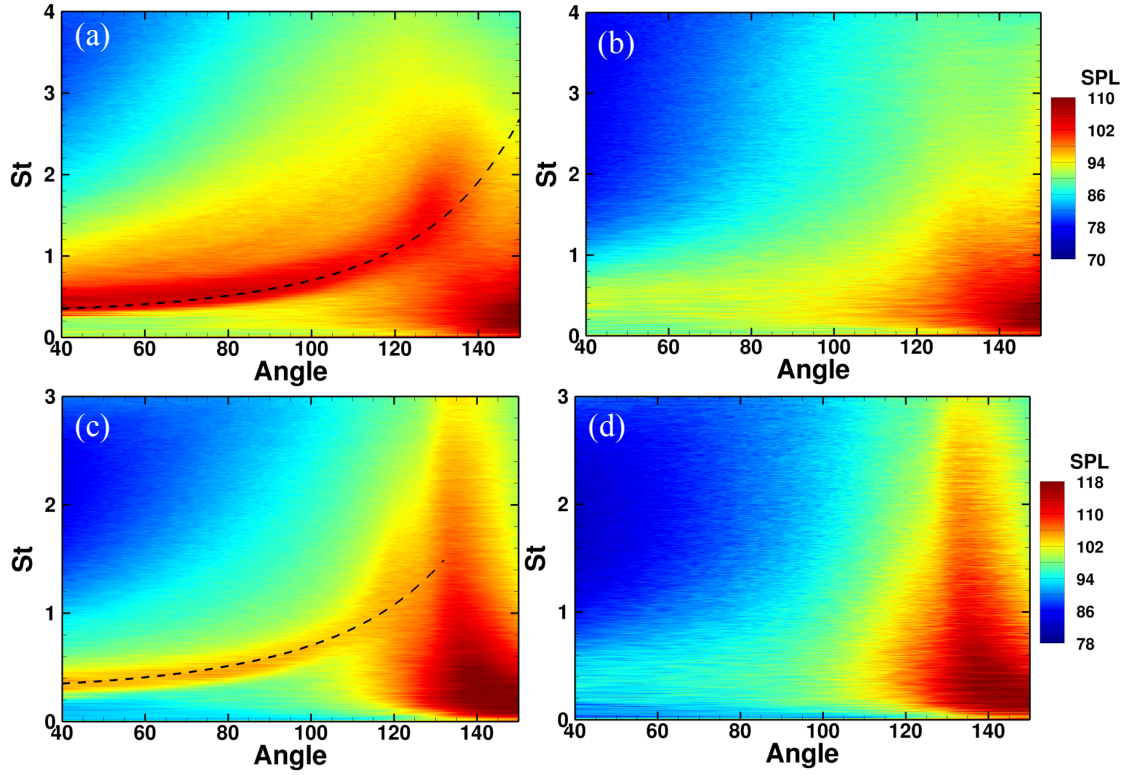
Figure 23. Sound pressure level distributions in the far field. (a)-(b). T_o/T_{amb} = 1.0 (cold jet). (c)-(d). T_o/T_{amb} = 2.0. Figures on the left are shock containing, and on the right are shock free. The dashed lines are results from the broadband peak frequency model proposed by Harper-Bourne and Fisher [1] and also by Tam and Tanna [2].
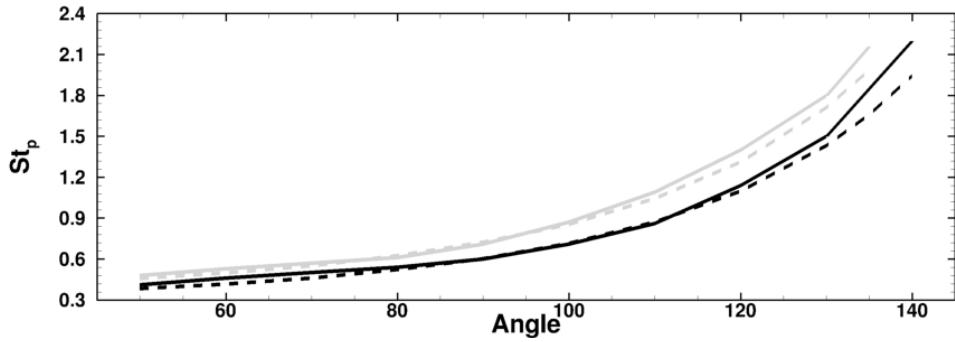
Figure 24. Comparison of shock-associated peak frequency with the prediction from the model given by Harper-Bourne and Fisher [1] and also by Tam and Tanna [2] at two far-field radii. Solid lines: LES prediction. Dashed lines: model predictions. Black lines: r = 47D. Gray lines: r = 1000D.
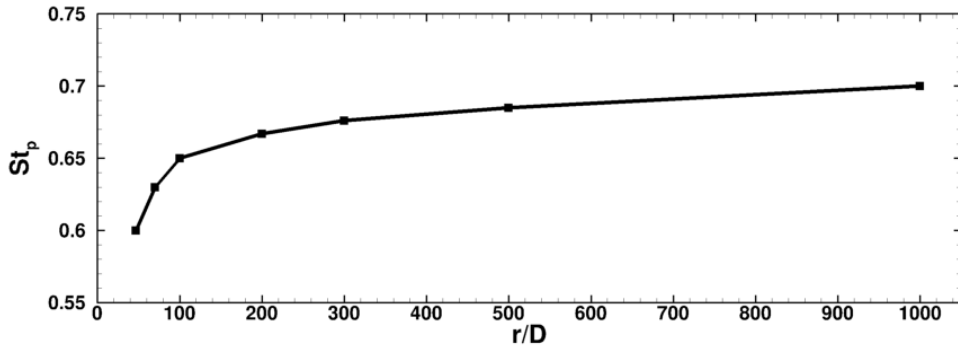

Figure 25. Peak frequency of shock-associated noise at the sideline angle versus the far-field distance at the cold jet condition.
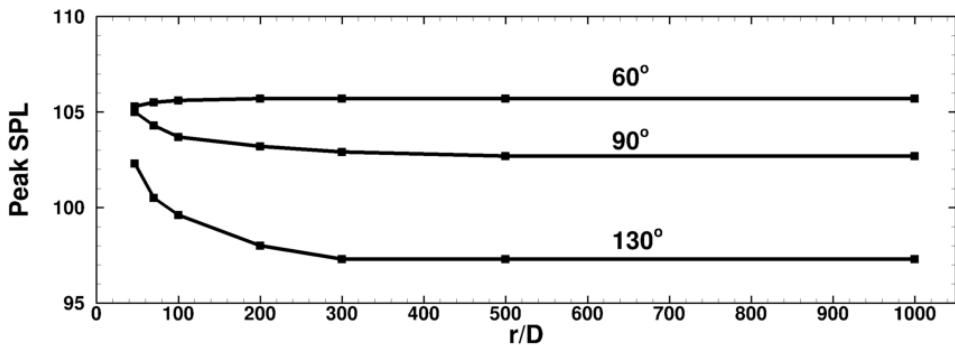

Figure 26. Peak level of the shock-associated noise at three radiation angles versus the far-field distance at the cold jet condition. All noise levels are scaled to the level at r = 47D with the scaling law of $1/r$.

29
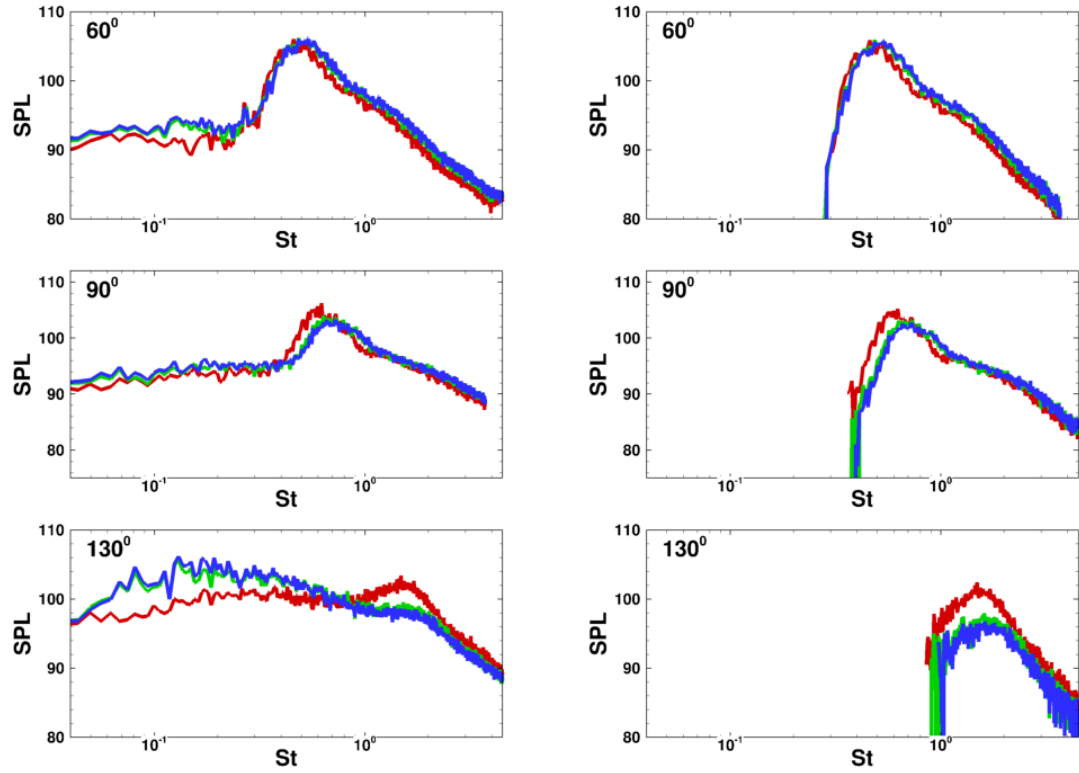
Figure 27. Impact of the far-field distance on the noise profiles. Left figures are total noise, and right figures are shock-associated contribution. Red lines: far field at r = 47D. Green lines: far field at r = 200D. Blue lines: far field at r = 1000D. All noise levels are scaled to the level at r = 47D with the scaling law of $1/r$.